Universiteit Utrecht

Royal Netherlands
Meteorological Institute
*Ministry of Infrastructure and the Environment*

# APPLYING GRAPH THEORY FOR A MORE CONSISTENT ESTIMATE OF THE BOUNDARY LAYER HEIGHT

*Mixing layer height retrieval using ground-based lidar measurements*

Marco de Bruine

Supervisors: ir. A. Apituley & dr. C.H. Tijm-Reijmer

## ABSTRACT

The height of the atmospheric boundary layer, or mixing layer (MLH) is an important parameter for understanding the dynamics of the atmosphere and dispersion of air pollution. MLH can be retrieved from lidar or ceilometer backscatter data. These instruments use aerosol concentration as tracer for MLH. This is possible because the main sources of aerosols are situated at the surface and exchange between mixing layer and free atmosphere is limited. Subsequently, high aerosol concentrations are associated with the mixing layer and low aerosol concentrations with the free atmosphere. Tracking MLH can be challenging in complex cases, such as under the presence of residual layers of air pollution or during periods of fog or rain. Various algorithms have been proposed, but a common feature in these algorithms is that the techniques are applied to each timestep individually, possibly resulting in incoherent estimates of MLH i.e. with unrealistic jumps in time.

Based on the gradual development of MLH, a new method called 'Pathfinder' is presented. It applies graph theory to evaluate multiple timesteps simultaneously, leading to a more consistent and gradual estimate of MLH. With the use of Dijkstra's shortest path algorithm (Dijkstra, 1959) the evolution of the MLH is tracked combining as much strong gradients as possible, given that subsequent estimates are within a certain vertical range of each other. The search is guided by restrictions based on features like clouds and residual layers.

Excellent agreement is found with windprofiler retrievals for a 12-day period in 2008 ($R^2$=0.90) and visual judgment of lidar data during a full year ($R^2$=0.96). We find that the new approach outperforms other backscatter lidar based-algorithms, especially during morning development and afternoon transition of MLH.



## ACKNOWLEDGMENTS

I would like to thank the following people for their support in my thesis: Arnoud Apituley for guiding me in my first venture into the world of climate science outside the lecture halls and giving me the opportunity to present my research at the ACTRIS 4$^{th}$ General Assembly in Clermont-Ferrand, Carleen Tijm-Reijmer for ensuring the quality of my work and greatly improving my writing skills with amazingly detailed feedback, Fred Bosveld for the brainstorm sessions and meteorological insights, Henk Klein Baltink and Marijn de Haij for supplying windprofiler, LD-40 ceilometer data and Dave Donovan answering the many questions I had on the UV-lidar.

# CONTENTS

# INTRODUCTION

The atmospheric boundary layer is the lowest part of the atmosphere where most of the interactions between surface and atmosphere take place. Therefore, knowledge of the processes and mechanisms taking place in this layer is essential in meteorology and climate science. One of the characteristics of the boundary layer is its height, also called mixing layer height (MLH). It is an important parameter affecting e.g. near-surface air quality. It governs the volume of air into which pollutants are emitted and dispersed. Primarily determining concentrations of aerosol and other gaseous species, it is an important parameter in predictions of pollution and smog. Additionally, different meteorological phenomena are determined by processes in the boundary layer, like the (dis)appearance of fog, formation of (strato)cumulus clouds, dew and frost. Knowledge of the MLH, is therefore of key importance for realistic representation of the atmosphere by weather forecasting models and climate predictions.

Several methods exist to observe MLH. Instruments used for this include the lidar, radiosonde, and windprofiler. Lidar measurements use aerosol concentration as tracer for MLH, which is possible because the main sources of aerosols are situated at the surface. These concentrations are relatively well-mixed by the turbulent motions in the mixing layer. But exchange between mixing layer and free atmosphere is limited. As a consequence, high aerosol concentrations are found in the mixing layer and low aerosol concentrations are found in the free atmosphere. This difference in aerosol concentrations can be used to determine MLH.

Advantages of using lidar for the observation of MLH is the high temporal and vertical resolution combined with a large measurement range from the ground up to possibly over 10 km into the atmosphere. Also, lidars can operate continuously and unattended for long periods. Next to that, the costs of lidars and ceilometers are relatively low. Many lidars are operated throughout Europe (and the rest of the world) by different institutes and for different purposes. By integration of these instruments into a network, MLH can be monitored over large areas.

But to produce useful, consistent and harmonized datasets with such a lidar network, standardization of the instruments and/or algorithms is needed. Several collaborations of national meteorological institutes already exist, e.g. TOPROF which aims to create an operational ground based profiling with ceilometers, lidars and microwave radiometers for improving weather forecasts or E-PROFILE in which a framework is developed to exchange lidar backscatter data.

This research proposes a new algorithm that can be standardized and applied to different lidars and ceilometers. This ‘Pathfinder’ algorithm is based on graph theory and Dijkstra’s (1959) shortest path algorithm for graphs.

To understand the rationale behind the new algorithm and the results of this research background information on the boundary layer is given in chapter 1. Chapter 2 describes different instruments used for boundary layer observations as well as the methods to derive MLH. Next to lidar, the radiosonde and windprofiler. In chapter 3, a more detailed description of existing lidar MLH detection methods is given. This includes the more general gradient, wavelet covariance transform and variance method used in different algorithms, but also the STRAT2D method which uses image pattern recognition called Canny edge detection. Chapter 4 presents the Pathfinder method and gives a detailed description of the different steps followed by this method. Results from this new method applied to the observations of a UV-lidar are discussed in chapter 5. It consists of three case studies, a 12-day comparison to other instruments and a full-year comparison against manually derived MLH estimates. The chapter is concluded with sensitivity test and application to other lidars. A summary with final conclusions and recommendations for future research are given in chapter 6.

# 1. THEORY

To interpret the lidar observations and judge the results of MLH estimates, it is necessary to understand the structure of the atmospheric boundary layer and its dominant mechanisms. It is impossible to treat every known aspect of the boundary layer here, but this section gives a short introduction covering the most important aspects.

## 1.1. Atmospheric boundary layer

The atmospheric boundary layer (ABL) is roughly the lowest 10% of the troposphere although it can vary in depth between approximately 100 meters to 2-3 kilometres in the mid-latitudes. It is the part of the atmosphere that 'directly feels' the presence of the surface. Response to effects of the surface is usually in the order of hours. Above this layer is the free atmosphere (FA) which is only influenced by the surface on longer timescales, typically a day or more.

Many different definitions exist on what the ABL precisely is, but none of those definitions are comprehensive or exact and some are rather ambiguous. Stull (1988) defined the ABL as "*that part of the troposphere that is directly influenced by the presence of the earth's surface, and responds to surface forcings of about an hour or less*". In general, these definitions refer to the fact the earth's surface influences the atmosphere directly above and indicate that the time scale of response is short. However, they leave unclear of what mechanics are behind this influence and what the impact of different timescales is.

A more complete but rather long definition is given by Garratt (1992): "*A useful working definition identifies the boundary layer as the layer of air directly above the Earth's surface in which the effects of the surface (friction, heating and cooling) are felt directly on time scales less than a day, and in which significant fluxes of momentum, heat or matter are carried by turbulent motions on a scale of the order of the depth of the boundary layer or less."* In this definition the key feature behind the mechanics in the boundary layer is indicated by the words 'turbulent motions'. The dominant presence of turbulence sets the ABL apart from the rest of the atmosphere. Therefore, insight in the causes, effects and characteristics of turbulence in the ABL are vital in understanding the boundary layer.

Two mechanisms can be responsible for causing turbulence: buoyancy and mechanical wind shear. Buoyancy is mainly caused by the absorption of incoming solar radiation by the earth's surface. This is one of the elements of the energy budget at the surface. The other elements are the absorbed radiation from the atmosphere, radiation emitted by the surface, turbulent fluxes of sensible heat and latent heat and the heat flux into the bottom. When the surface receives more heat from the incoming radiation of the sun (or atmosphere) than it loses by the other fluxes, the temperature of the surface increases. If the temperature at the surface is higher than the air above, the air at the ground will be less dense than the surrounding air and positively buoyant. This causes convection which manifests itself in thermals of warm air rising from the ground. These thermals stir up the atmosphere and create turbulence in the ABL. In the presence of clouds, convective instability can be caused at the top of the boundary layer by radiative cooling. As a result, a second kind of thermals is created with cool air sinking down. Both mechanisms often occur simultaneously.

Wind shear is the result of frictional drag of the air against the earth's surface. In case this shearing stress is strong enough, it creates disturbances and waves that keep growing in amplitude until they break and cause turbulence. This is called shear instability or Kelvin-Helmholtz instability. Higher up in the atmosphere, similar effects can be observed in the form of Kelvin-Helmholtz clouds. In statically stable stratified situations, the stratification prevents disturbances to grow and turbulence to arise. The relative strength of the wind shear compared to the strength of the stratification determines the characteristics of the ABL. This ranges from situations being nearly completely non-

turbulent to situations with still considerable mixing. This balance between buoyancy and shear stress is quantified in the Richardson number, which contains a ratio between the two mechanisms.

Under a critical threshold, the stratification is no longer capable of withstanding the shear forces and mechanical turbulence is formed. The Richardson number can thus be used as an indicator of turbulence and boundary layer height. A technique using the Richardson number to estimate the height of the boundary layer is described in section 3.2.

As turbulence mixes the air, heat, water and pollutants in it are mixed as well. In boundary layers driven by convection, the concentrations of these quantities are usually well-mixed and fairly constant. This characteristic can be used to distinguish this layer from the FA. Measurements of the vertical profiles of temperature and moisture can be seen in figure 1.1. The absence of turbulence in the FA atmosphere also causes limited exchange between the two air masses.

This distinction also applies to other (mainly shear driven) boundary layers, as long as turbulence persists. Mixing in these boundary layers however, can be intermittent or even absent leading to an uneven distribution of heat, water or pollutants within the ABL.

As buoyancy is a dominant process in mixing, the sun is the driving force behind turbulence during daytime. This gives rise to two completely different ABL regimes: the stable (nocturnal) boundary layer and unstable (diurnal) convective boundary layer. The following sections will provide a short description of the two regimes and will also zoom in into the entrainment zone, where mixing between the ABL and FA takes place. To conclude this chapter the influence of clouds on the boundary layer is discussed.

### 1.1.1. Convective boundary layer

Buoyancy and resulting convective motion is the dominant mechanism for turbulence in the convective boundary layer (CBL) also called the mixing layer (ML) as the convective motions in the layer mix all quantities like heat, water or pollution and distribute them evenly over the CBL. As explained above, solar radiation is the main cause for the buoyancy and the CBL forms during daytime. A typical diurnal cycle of the CBL at the mid-latitudes is shown in figure 1.2

During daytime the surface heats up by solar radiation. When the temperature of the surface becomes higher than the air above positively buoyant air starts to rise up and form the ML. Initially this layer is very shallow, but grows as more heat is added to it. Two different mechanisms are responsible for the growth of the ML: encroachment and entrainment. Encroachment is the most important of the two mechanisms as this process is responsible for 80-90% of the variation in the

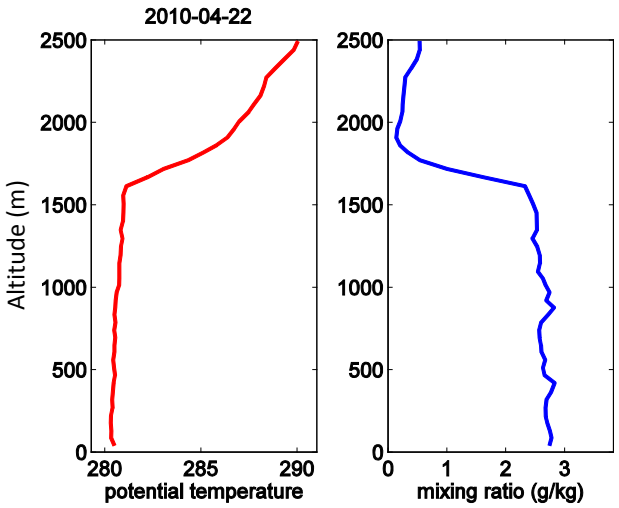


***Figure 1.1. 12 UTC Radiosonde of 22 April 2010 at De Bilt. An example of vertical profiles of potential temperature and mixing ratio. Clearly visible is the distinction between the boundary layer and the free atmosphere above. With the ABL being well-mixed the potential temperature and mixing ratio are nearly constant up to an altitude of 1700 meters. After that there is a transition into the FA which is much warmer and has a stable stratification. The FA is also much drier.***

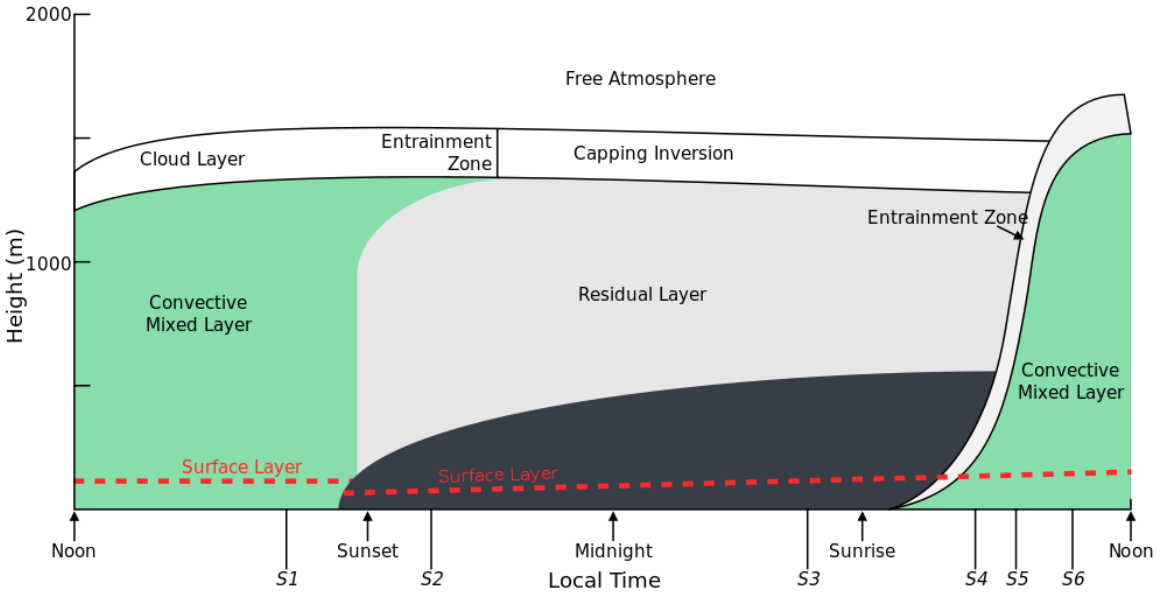


***Figure 1.2. Theoretical structure and diurnal cycle of the atmospheric boundary layer (ABL) at the mid-latitudes. Different regimes and regions within the ABL are shown. Adapted from Stull (1988).***

height of the ML (Stull, 1976; Boers et al., 1984). With encroachment the height of the ML increases due to air rising from the surface, whereas entrainment increases the height of the ML by capturing air from the FA by turbulent mixing. The main difference between the two processes is that, in contrast to entrainment, with encroachment there is no mixing of air from the FA and ML. A brief explanation of both processes is given below, starting with encroachment.

As the temperature of the surface is higher than the air above, it is positively buoyant and rises until it reaches an altitude with the same potential temperature. The resulting mixing between the surface and the altitude reached by the rising air leads to a constant (potential) temperature $\theta_L$ in this layer. In the example shown in figure 1.3, if the temperature of the ML $\theta_L = \theta_1$, the height of the ML (MLH) will be $z_1$. The amount of heat needed to warm this layer from $\theta_0$ to a constant temperature $\theta_1$ is indicated by the shaded area.

As $\theta$ increases rapidly with height in the nocturnal temperature inversion (between $\theta_0$and $\theta_1$) a significant amount of heat is needed to increase the MLH. This inhibits quick growth of the ML. When the nocturnal temperature inversion is broken down and the ML gained a temperature of $\theta_1$ and reaches up to altitude $z_1$, the ML can grow more rapidly. Because $\theta$ increases less with altitude (i.e. between $\theta_1$and $\theta_2$), less heat is needed to increase the MLH. This allows for rapid ML growth. After

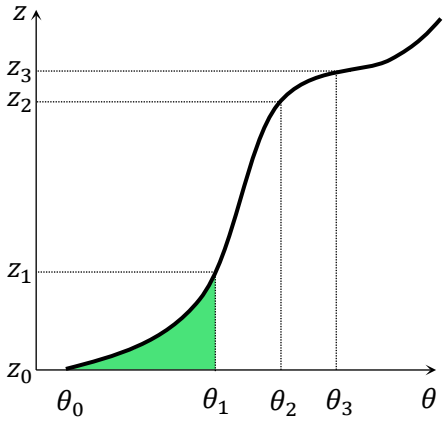


***Figure 1.3. Graphical representation of encroachment. Shaded areas indicate the amount of heat needed to increase the temperature in a layer of air up to a certain height. The shaded area represents heat needed to attain a layer of constant potential temperature $\theta_1$. By having this temperature, the ML will reach to height $z_1$. The blue area under the nocturnal temperature inversion is relatively broad and mixing height will grow slowly when the temperature increases from $\theta_0$ to $\theta_1$. In contrast, with the (smaller) temperature increase from $\theta_1$ to $\theta_2$ yields a much higher increase of mixing height from $z_1$ to $z_2$. A similar temperature increase $\theta_2$ to $\theta_3$ at the capping inversion needs more heat and yields only a small increase in ML height from $z_2$ to $z_3$.***

the height of the ML has reached the capping inversion at $z_3$, the depth of the layer will only grow slowly by encroachment as $\theta$ increases rapidly with height at this altitude. A lot of heat is needed to further increase the MLH.

To summarize encroachment, the height of the ML layer is determined by the vertical profile of $\theta$ and the potential temperature at the surface $\theta_S$ and is located at the altitude where $\theta = \theta_L$. The warming and growing of the ML by mixing heat from the surface is the process called encroachment. This process does not affect the temperature profile above the ML and therefore, the ML will never grow higher than the intercept of the potential temperature of the ML $\theta_L$ and the vertical profile of $\theta$ by encroachment.

Additional growth of the ML is caused by a process called entrainment. In this process non-turbulent air of the free atmosphere is captured by the turbulent air of the ML. Turbulence in the ML is organized in plumes and thermals of rising warm air. During their ascent in the ML the thermals keep gaining speed due to their positive buoyancy, leading to typical vertical velocities of 1-2 $ms^{-1}$. When reaching the potentially warmer air of the FA, their buoyancy becomes negative and the thermals will slow down, but not stop their ascent immediately because of the gained momentum. Instead they will penetrate into the FA, before sinking back into the ML. This process is called overshoot. Because the FA is not turbulent, thermals do not disperse there. Instead, the thermals remain mostly intact and sink back into the ML. But because of the overshoot of thermals into the FA, FA air is pushed aside and down into the ML. Opposed to the overshooting air, this FA air now resides in a turbulent environment and dissipates quickly. This assimilation of air by entrainment causes the growth of the ML as the air from the ML will occupy the volume of the FA taken up by the ML. It is important to realize entrainment is a one-way process: the less turbulent air from the FA is mixed into the turbulent air of the ML, but not the other way around. The air from the ML and all constituents like heat water and pollution are trapped in the ML. As opposed to encroachment, entrainment does influence the air above the ML by the overshooting thermals and alters the temperature profile as shown in figure 1.4.

As subsequent thermals reach slightly different heights and plumes of entrained air disperse at a somewhat different rate, the height of the ML fluctuates quite rapidly and it is hard to determine an exact MLH. Usually, the region of overshooting thermals and entraining air from the FA is called the entrainment zone which can be hundreds of meters thick.

As shown in figure 1.2, ML growth rates vary substantially during the day, but are largest at the end of the morning after the nocturnal temperature inversion has broken down and heat from the surface has to be distributed over a relatively thin layer. As surface heating by solar radiation drives the convection in the ML, growth rates also vary during the year. In the mid-latitudes, most common

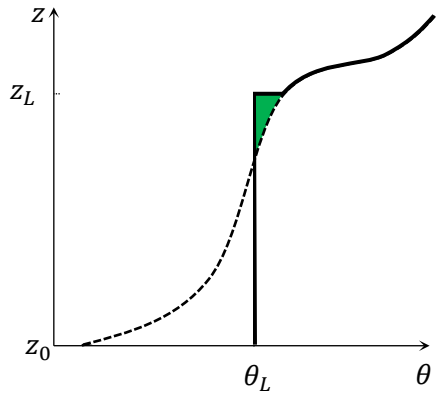


***Figure 1.4. Graphical representation of entrainment. During the day, the stable early morning temperature profile (dashed line) changed into a profile with a constant θ up to a certain altitude (solid line). As entrainment is not caused by heating of the ML, growth of the ML by this process leads to a typical temperature profile with a sharp temperature step at the top of the ML. In contrast to encroachment, ML growth by entrainment exceeds the intercept of $\theta = \theta_L$.***

growth rates are between 100 and 300 m/hr, but during spring and summer values above 400 m/hr can be observed with peak days up to about 1000 m/hr (Baars et al., 2008). A typical MLH in the mid-latitudes is 1-2 km.

At the end of the day, incoming solar radiation will diminish and the surface radiation balance will become negative. The surface starts to cool down and with this, the driving force behind the convective turbulence vanishes. Without sufficient forcing, the turbulence in the mixing layer will decay. As the surface cools, a stable layer starts to develop from the surface upward. The air of the ML above this stable layer is no longer in contact with the surface and classified as residual layer. However, this transition is not abrupt and some thermals may still be rising while the lower part of the layer has already become stable. The stable part near the surface is the beginning of the nocturnal boundary layer.

### 1.1.2. Stable (nocturnal) boundary layer

When the sun sets, the surface receives less radiation than it emits and the energy balance will be negative. The surface will start to cool down and when it becomes colder a surface-based temperature inversion starts to develop. Convection will seize and wind shear is the only source for turbulence. This regime is called the stable boundary layer (SBL), or nocturnal boundary layer (NBL) because it most often occurs at night.

The most shallow and stable boundary layers are found in completely cloud free nights, with low wind speed. On such nights, the surface can freely emit the stored heat and will not receive radiation emitted by clouds and thus cool down very quickly. The stratification will be very stable and will dampen any turbulent motions before much mixing can occur. On such nights, the boundary layer can be limited to the lowest tens of meters above the surface. On cloudy nights (with high wind speeds) however, with a neutral stratification and ample wind shear for turbulence production the NBL can still reach up to altitudes in the order of 1 km.

The height of the SBL is much harder to quantify (and measure) than the ML as it has no clear boundary. Instead, it usually blends gradually into the residual layer. Definitions to mark the depth of the SBL are, for example, the lowest height where the lapse rate becomes adiabatic ($\partial\theta/\partial z = 0$) or where the wind speed $\vec{v}$ is maximum.

Determining a mixing layer (in direct contact with the surface) in the SBL might be even harder. Turbulence can have an intermittent character with individual episodes with mixing followed by periods without any turbulence at all. Determination of a mixing height will depend on what time scale is used to define contact with the surface.

### 1.1.3. Clouds in the boundary layer

In previous sections clouds were only mentioned incidentally, but the presence of clouds has a large impact on the structure of the boundary layer. Additional buoyancy can result from radiative cooling at the top of clouds or latent heat release as water condenses in the clouds. The energy balance at the surface is also influenced by the presence of clouds as they can absorb solar radiation and emit infrared radiation.

Clouds in the boundary layer mainly consist of three cloud types: cumulus, stratocumulus and stratus clouds. Next to that, fog is a typical boundary layer phenomenon.

Cumulus clouds form on top of the boundary layer as thermals rise above the lifting condensation level (LCL). These clouds often form in the negatively buoyant part of the thermal overshooting in the FA. Forced cumulus do not reach the level of free convection (LFC) and only exist while there is forcing from the thermal. As a result they are very shallow. Active cumulus clouds form when the

cloud top reaches LFC. Reaching this level, the cloud becomes positively buoyant and is now controlled by its own dynamics and interaction with the environment. These clouds can vent ML air into the FA. Active cumuli are not very shallow but their vertical dimensions are on the same order as the horizontal dimensions. When active clouds stop withdrawing air from the ML, they are classified as passive cumulus. Like active cumulus, they can still be growing, but they are no longer venting ML air into the FA. It is not detached and no longer part of the ML.

Stratus and stratocumulus clouds in the ML can form by a variety of forcings. But as these cloud decks usually cover most of the sky these must forcings must be maintained without strong solar heating of the surface. Examples of these processes are surface based convection due to advecting cold air over a warm surface. Strong winds can also cause mixing and form stratocumulus clouds in the ML. Radiative cooling at cloud tops creates 'reversed' thermals of cold air that sink down and can maintain an existing stratocumulus cloud deck. The clouds triggering these thermals are only considered to be part of the ML when the thermal extend to the surface.

As clouds can be the result of convection from the ground or mixing driven by radiative cooling at the cloud top, cloud-topped boundary layers can be summarized into three categories (Garratt, 1992). A schematic overview is given in figure 1.5. In type A, the clouds are fully coupled to the air below by turbulent mixing and the ML extends from the surface to the cloud top. The turbulence can be driven by convection from the ground or cloud top radiative cooling reaching the surface. In type B, two or more cloud layers exist at the same time. In this situation, the lowest cloud layer is coupled to the surface, whereas the other is not in contact with the surface. These higher cloud layers are elevated mixed layers driven by radiative cooling. The lowest cloud layer is driven by either convection from the ground or radiative cooling, like the cloud in type A. Only one cloud layer exists in type C, but it is decoupled from the surface. There might be turbulent mixing from the ground, but the ML does not extend to the cloud layer above.

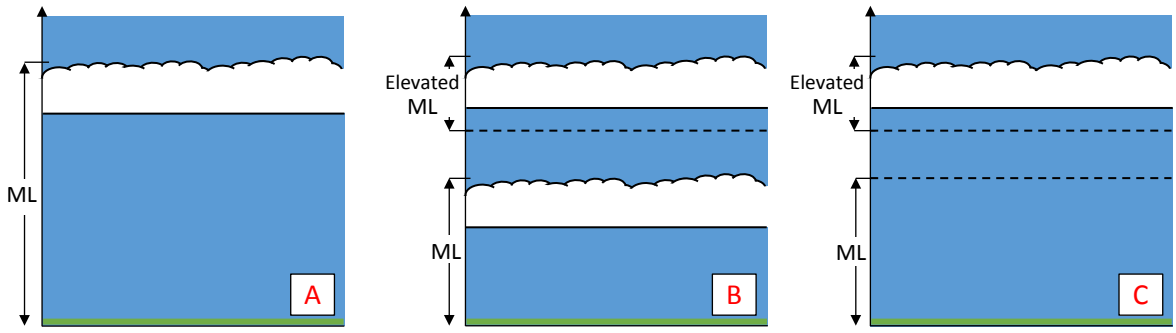


**Figure 1.5** ***Schematic representations of 3 cloud-topped boundary layer categories, adapted from fig 7.2 in Garratt (1992). Type A, fully coupled cloud layer, with the ML extending from surface to the clouds; type B, multiple cloud layers with a ML extending to the lowest clouds and type C, a decoupled cloud layer with the ML not reaching the cloud layer.***

## 1.2. Graph theory

For the derivation of MLH, the new method proposed here translates lidar measurements into a graph. This enables the use of Dijkstra's shortest path algorithm (Dijkstra, 1959) to calculate the evolution of the MLH. Because this algorithm is the core of the new method, this section gives a short introduction to graph theory and Dijkstra's algorithm.

Graphs are a mathematical representation of a set of objects with links between them. The interconnected objects are usually called vertices. The connections between them are called edges. Other features in graphs can be weights assigned to edges or the direction of edges.

Problems that can be translated into graphs are people and their connections for example. In such a graph the vertices would represent different people and the edges would represent e.g. friendships between them. Another example is the connection of cities by the roads between them. In this graph the cities would be represented by the vertices and the roads are translated into edges. The lengths of the roads can be incorporated by added weights to the edges and one-way road can be symbolised by adding a direction to a certain edge.

Considering the example of cities and roads, an interesting problem is to determine the shortest route from city A to B. These problems are called 'shortest path' problems and many techniques exist to solve them. The most straightforward way to determine the shortest path between two vertices is to check every possible path and select the shortest one from all the possibilities. This is however a very inefficient method and takes considerable computing power. In particular if the number of vertices increases and if there are many edges between them. One of the most efficient algorithms to find shortest paths is Dijkstra's algorithm (1959).

The goal of the algorithm is to construct a so-called tree. This tree consists of all vertices of the original graph, but only the edges needed for the shortest paths are left. An example can be seen in figure 1.6.

The basis of Dijkstra's algorithm is the addition of edges individually to make a complete tree of shortest paths. Adding these paths one-by-one and rejecting all other possibilities to this tree ensures no paths are disregarded that could improve the result. On the other hand, building the tree by the shortest known paths also guarantees that the selected paths are indeed the shortest ones, although not all paths leading to a vertex are known yet. When all vertices are processed in this selection process all shortest paths from one vertex to all the other vertices are known.

To compute the tree using Dijkstra's algorithm the vertices and edges are both distributed over three sets. For the vertices (in the example these sets are labelled X, Y and Z respectively) these sets are:

X Vertices for which the shortest path is known,
Y Vertices for which a path is calculated, but it is not yet clear whether this is the shortest path,
Z Remaining vertices not yet connected to the starting vertex.

The three sets of the edges (labelled I, II and III) are structured in a similar manner:

I Edges occurring in the shortest paths to vertices in set X,
II Edges of paths leading to vertices in set Y, but not clear if these are the shortest possible,
III Edges that are not yet considered or rejected as shortest path

To clarify the way the algorithm works we will apply the algorithm to the graph shown in figure 1.6. At the beginning of the calculations all vertices are placed in set Z and all edges are placed in set III as no paths are yet considered. Suppose we would like to know the shortest paths from vertex A to all others.

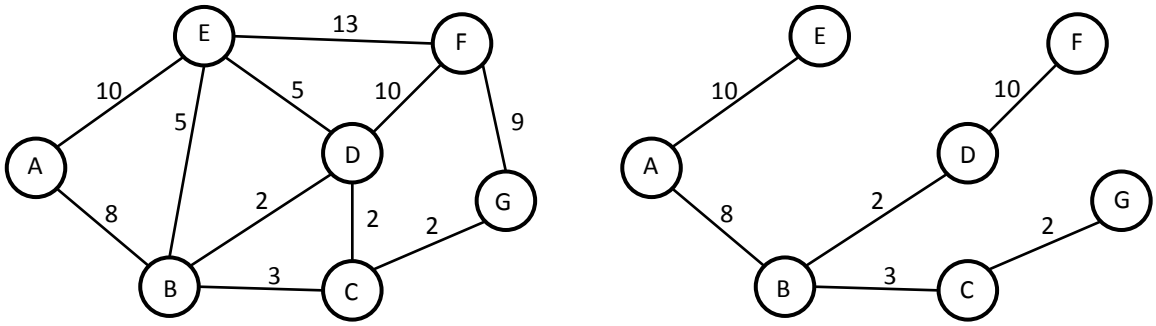


*Figure 1.6. left) Visual representation of the graph in the example with all vertices and edges. right) Corresponding tree of shortest paths leading from vertex A to the other vertices, edges not part of the shortest paths are deleted.*

Step 0 As vertex A is the starting point, this vertex is automatically placed in set X because the shortest path to this node is now 'known', being 0.

Step 1A The first step in the algorithm is to evaluate the outgoing branches from vertex A. These are the edges {A,B} and {A,E}. We write down these new paths in the overview shown in table 2.1. For the new paths connected to vertex A, we note the vertex from which the edge originated and corresponding (total) length to vertex A in the following way: [ *vertex* , *total length* ]. For the connection between vertices A and B, this is [A, 8]. As vertices B and E are now connected to vertex A we move these to set Y. As we have no previous paths yet, the corresponding edges are the shortest paths automatically and are moved from set III to set II.

Step 1B From the vertices belonging to set Y the one with the shortest path to vertex A is selected. This is vertex B. This follows from the overview as the notation in row 1 corresponding to this path has the lowest total length. Vertex B is moved from set Y to set X and the edge {A,B} is moved from set II to set I. This vertex and edge are now permanently added to the network of shortest paths.

Step 2A We now repeat the procedure and evaluate the outgoing branches from vertex B, being {B,A}, {B,C}, {B,D} and {B,E}. It is unnecessary to look at the edge connecting to vertex A, as the shortest path to that vertex is already known. More generally, only the edges leading to vertices in currently in set Y and Z should be evaluated. For edges {B,C}, {B,D} and {B,E} are written down in the overview. No paths to vertices C and D were known yet, so these are moved to set Y and corresponding edges to set II. For vertex E a possible path was already known, the question is whether the new path is shorter. The path from vertex A to E through B has a length of 13, composed of the path leading to B with length 8 and the new edge with a length of 5. This exceeds the length of the previous path and the edge {B,E} is rejected and remains in set III.

Step 2B Set Y is now composed of vertices C, D and E. We again select the vertex with the shortest path to A. Both vertices D and E have a total length of 10. With a path length being equal, it does not matter which vertex is selected. This will not change the outcome of the algorithm. We will select vertex D and move it to set X and corresponding edge to set I.

Step 3A From vertex D there are edges leading to nodes B, C, E and F. Like before, vertex B belongs to set X, so edge {D,B} is ignored in this step. Analogous to the previous step, new paths to vertices from set Y and Z are calculated and added to the overview. Vertex F has no connections yet and is automatically added to set Y and corresponding edge moved to set II. The new path to node C has a length of 12 and is longer than the path via B and is rejected. The same holds for the new path to E.

| Set X | Set Y | Set Z |
|---|---|---|
| - | - | all |
| A | - | B-G |
| A,B | E | C,D,F,G |
| A,B,D | C,E | F,G |
| A,B,D,E | C,F | C,G |
| A - E | F | G |
| A - E, G | F | - |
| all | - | - |

*Table 2.1a . Tracking of the different sets of vertices.*

| step | | A | B | C | D | E | F | G |
|---|---|---|---|---|---|---|---|---|
| | | [A,0] | | | | | | |
| 1 | A | | [A,8] | n.a. | n.a. | [A,10] | n.a. | n.a. |
| 2 | B | | | [B,11] | [B,10] | [B,13] | n.a. | n.a. |
| 3 | D | | | [D,12] | | [D,15] | [D,20] | n.a. |
| 4 | E | | | | | | [E,23] | n.a. |
| 5 | C | | | | | | | [C,14] |
| 6 | G | | | | | | [G,23] | |
| | F | | | | | | | |

*Table 2.1b. Tracking of the (temporary) shortest paths leading from the different vertices. The notation explains the total path length and first predecessor of the edge named in the column head.*

Step 3B In set Y are now vertices C, E and F, of which vertex E has the shortest path to vertex A with a length of 10. Vertex E is moved to set X and edge {A,E} is moved to set I.

Step 4A From vertex E there are 4 edges to vertices A, B, D and F. We will only take the new edge to vertex F into account because the other vertices belong to set X already. After comparison of the new(length 23) and previous (length 20) paths, the existing path is still the shortest and the new edge is rejected.

Step 4B Set Y now comprises vertices C, F and G. Vertex C has the shortest path and is moved to set X. Edge {B,C} is moved to set I.

Step 5A Vertex C is connected to vertices B, D and G. Similar to step 4A we now only consider edge {C,G}. This edge and vertex G were not yet connected and are automatically moved to set Y and set II respectively.

Step 5B Of the vertices in set Y, vertex G has the shortest path and is transferred to set X and corresponding edge {C,G} is moved to set I.

Step 6A From vertex G there are edges to vertices C and F. The shortest path to C is known so only the path to F is looked at in this step. The new path with a length of 23 is longer than the previous path and the edge remains in set III.

Step 6B Only vertex F is left in set Y and is moved to set X. Analogously only vertex {D,F} is left in set II and is moved to set I.

All vertices are now in set I, which means that the shortest paths from vertex A to all other vertices is known and the algorithm is done. With the recording of the different paths we kept track of the total path length and origin from which a new connection was made. If we want to know the shortest path from A to F we can backtrack as follows. Comparing the entries in column F of the overview it can be seen that the shortest path led from vertex D and had a total path length of 20. Now looking in column D it can be seen the shortest path was via vertex B. Again looking at column B it can be seen the shortest path was via vertex A. Adding this information, the shortest path can be reconstructed to {A,B,D,F}.

Even though the technique is 55 years old, Dijkstra's algorithm is still the most efficient algorithm to solve single source shortest problems for graphs with non-negative edge weights. In other words, finding the path with the lowest total cost/weight from one vertex to any other vertex in a graph, this algorithm uses the least computing power. Unfortunately, it is restricted to graphs with positive weights. This is due to the fact that paths are selected according to their total path cost from the starting vertex. Adding negative weights can change this ordering and causes the algorithm to fail.

# 2. MEASUREMENT TECHNIQUES

As the research field of atmospheric science developed, more and more measurement techniques were created for the many different quantities involved in weather and climate. Several of those can be useful in measuring the MLH. This section presents an overview of instruments used to measure the atmospheric boundary layer.

An overview of the most common instruments used for MLH measurements is shown in table 3.1. Next to these instruments, turbulence measurements are also used to estimate quantities as latent heat flux $H$, friction velocity $u_*$ and Obhukov length $L$. Many theoretical relations exist to estimate MLH and ML growth from surface observations. (e.g. Pul et al, 1994).

As lidar is the main instrument used in this study, a description in some detail of this instrument will be given in section 2.1. Next to that, radiosonde and wind profiler measurements are used to compare results in this study. A short description of these measurement techniques and methods to derive MLH are given in sections 2.2 and 2.3.

| Instrument | Advantages | Disadvantages |
|---|---|---|
| Radiosonde | - Extensive network with soundings on a regular basis<br>- In situ measurement of thermodynamic state<br>- In-situ measurements throughout vertical column<br>- Operation (nearly) independent of weather conditions | - Low temporal resolution, maximum of a few times per day |
| Lidar/ceilometer | - High temporal and vertical resolution<br>- Large network in existence | - Presence of tracer (aerosol) necessary<br>- Operation limited by weather conditions (fog, heavy precipitation) |
| Wind profiler | - Direct measurement of turbulence | - Low vertical resolution<br>- Operation limited by weather conditions (fog, heavy precipitation) |
| Mast | - Possibility of installing many different instruments<br>- In-situ measurement | - High costs<br>- Limited vertical range |
| Aircraft | - In-situ measurement | - High costs<br>- Lowest measurement height restricted by regulations |

***Table 2.1. Overview of different instruments used for boundary layer measurements. For each of the instruments, the most important advantages and disadvantages are summed up.***


***Figure 2.1. Picture of the LEOSPHERE ALS450 UV-lidar located at the remote measuring site of the Cabauw experimental site for atmospheric research (CESAR). This lidar operates at a wavelength of 355 nm with a temporal resolution of 30s and a vertical resolution of 15 meters.***

## 2.1. Lidar

A lidar (acronym for light detection and ranging) is an instrument using infrared, visible or ultraviolet light to detect atmospheric components invisible to radars or other equipment using other sounding wavelengths. A schematic overview of a lidar system is shown in the left panel of figure 2.2. To measure the atmosphere, the lidar emits laser beam pulses into the atmosphere to excite backscattering on scattering particles like aerosols, molecules or cloud and rain droplets. This backscatter signal is detected by a telescope receiver and sent to a photodetector and the results are stored on a computer. As the laser and telescope are located next to each other, the laser beam is outside the field-of-view (FOV) of telescope near the ground. As the FOV of the telescope diverges, the laserbeam and the FOV will first partly overlap and eventually fully overlap. The height of complete overlap is typically in the order of 100 meter for ceilometers and small lidars.

The intensity of the backscattered signal is proportional to the size of the particles and number concentration. This dependence on the size of the particles allows for identification of the different type scattering particles. Together with the dependence on the number concentration, aerosols, clouds and clean air can be identified. Using the intensity of the backscattered signal together with timing between emitting and receiving of the laser beam pulse, vertical profiles and layers of aerosol, clouds and clean air can be observed.

Characteristic for lidar measurements is the high sampling rate allowing vertical resolution in the order of typically 10 m or less and temporal resolution in the order of 30 s or less. Despite of the high vertical resolution, lidar also has a long range of penetration, possibly over 10 km into the atmosphere. This makes the instrument well suited for boundary layer research, e.g. vertical profiling of water vapour and trace gases or detection of clouds and layers of aerosols.

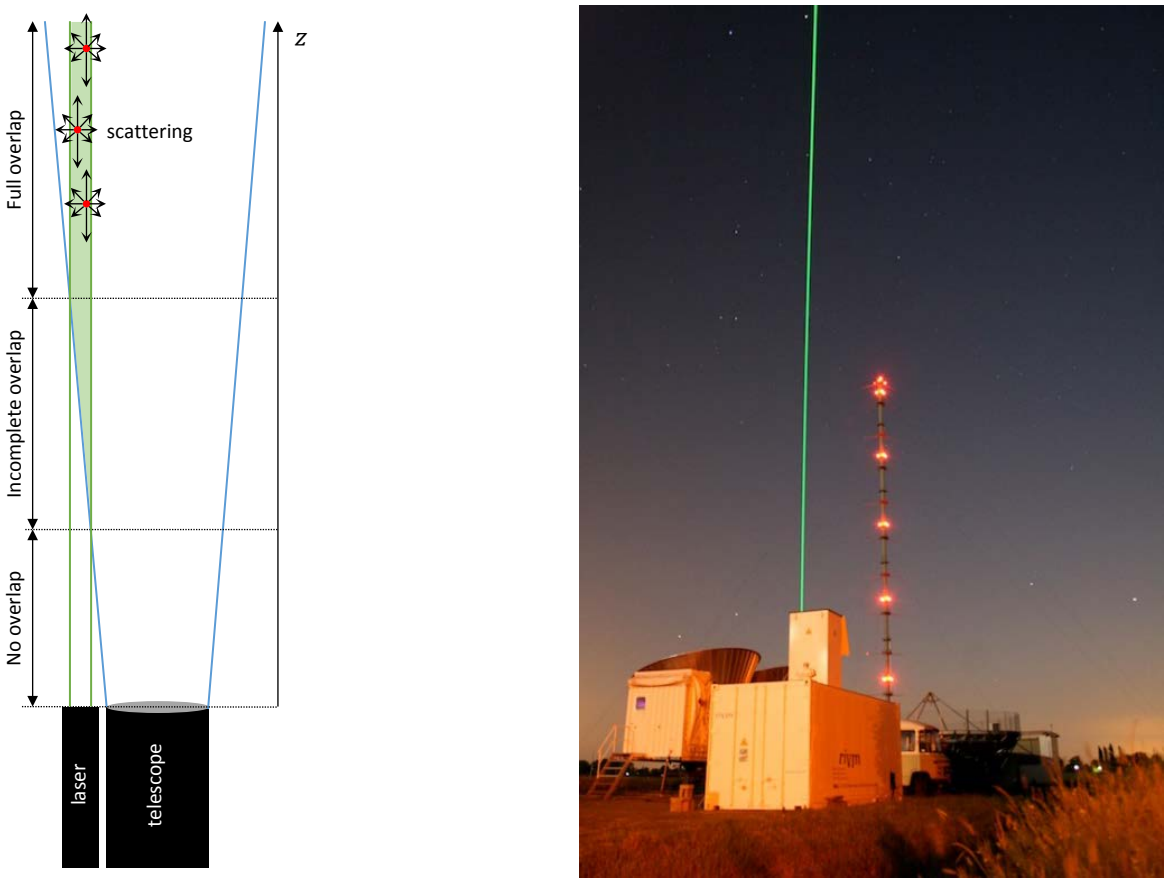


***Figure 2.2.Overview of a lidar system. left) Schematic representation of the lidar principle and explanation of the overlap region. Adapted from figure 1.2 in Noicolae and Talianu (2010). right) Picture of the CAELI Raman lidar at night emitting a laser beam. The light with a wavelength of 532 nm is visible as green light. This lidar is located at CESAR as well.***

The use of lidar measurements in boundary layer research relies on aerosol concentration which is used as a tracer for different air masses. Because the main aerosol sources are located at the surface, and exchange between ML and FA is limited, aerosols are confined within the ML. Subsequently, high aerosol concentrations are associated with air in the ML and low aerosol concentrations with air of the FA. Consequently, high backscatter is related to air in the ML and low backscatter to FA air. Exceptions are conditions in which polluted layers are transported over long ranges (up to thousands of kilometres in layers above the ML). Examples of these are plumes ashes brought into the atmosphere by volcanic eruptions or Saharan dust.

Scattering of light can be both elastic and inelastic. In case of elastic (Mie or Rayleigh) scattering, the wavelength of the light remains unchanged after the interaction of light with the scattering particle. In case of inelastic (e.g. Raman) scattering the wavelength of the light before scattering is different from the wavelength after scattering. Here we will consider elastic scattering only.

Mie scattering occurs in situations where the wavelength of the light is comparable to the scattering particle, as lidars use infrared, visible or UV light this means Mie scattering results from interaction of light with aerosol particles and rain or cloud droplets. Rayleigh scattering applies to the case when the scattering particle is much smaller than the wavelength of the scattered light. For lidar applications, Rayleigh scattering results from interaction with the molecules of the different gases in the atmosphere.

The (range corrected) lidar-detected signal $RCS$ for elastic scattering can be written as

$$RCS(\lambda, R) = C_S(\lambda, R)\ \beta(\lambda, R)\ T(\lambda, R)^2\ + b(\lambda, R), \tag{2.1}$$

where $C_S$ is a function specific to the instrument and corrects for properties of the internal optics that influence the detected light backscatter power, $\beta$ is the atmospheric backscattering coefficient, $T$ is atmospheric transmittance coefficient and $b$ is the background signal not originating from the lidar itself but from the sun or other sources. $T$ is squared in this equation as light emitted and scattered back to the receiving telescope has to travel the distance between the particle and the lidar twice. $R$ is the altitude of the probed volume and $\lambda$ is the wavelength of the emitted light by the lidar.

The atmospheric backscattering coefficient $\beta$ is important here as it is proportional to the backscattering cross section $\sigma_\pi$ and number density $N$ of scattering particles in the atmosphere, like atoms, molecules, aerosols, cloud droplets etc. $\delta R$ is the spatial resolution of the lidar and is the thickness of the probed volume:

$$\beta(\lambda, R) = \sigma_\pi(\lambda)\ N(R)\ \delta R \tag{2.2}$$

The dependence on $\sigma_\pi$ and $N$ allows us to identify different air masses by particle concentration as the backscatter intensity increases with increasing concentrations of scattering particles.

The expression for $T$ reveals itself as the Lambert-Beer law, which relates the attenuation of light to the properties of the medium through which the light is travelling:

$$T(\lambda, R) = \exp\left[-\int_0^R \alpha(\lambda, r)dr\right]. \tag{2.3}$$

Here, $\alpha$ is the atmospheric extinction coefficient. All interactions between the light and the scattering particles are captured in this coefficient and the exact value depends on the composition of the air and the wavelength of the light. These dependencies are similar to the backscattering coefficient discussed above.

Figure 2.3 shows an example of the vertical profile of potential temperature observed by radiosonde and the corresponding vertical profile of received backscatter measured by lidar. Both measurements were taken simultaneously. In this example, the ML reaches up to about 2000 meters as can be observed from the vertical profile of the potential temperature. The observed profile by

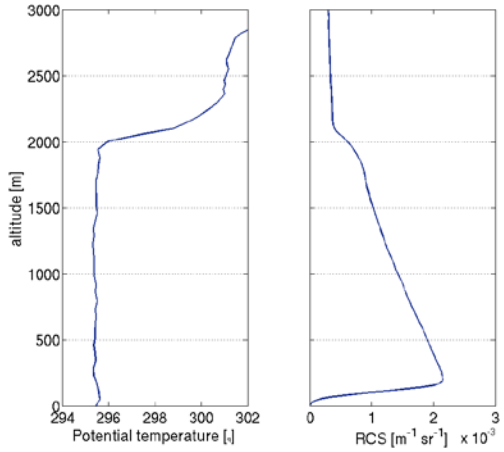


***Figure 2.3. Comparison of the vertical temperature profile measured by radiosonde and the RCS measured by UV-lidar. Both measurements are taken at 16 UTC on 8 May 2008, at Cabauw during the EUCAARI IMPACT campaign.***

the lidar can be divided into 4 different regions. From the ground to about 200 meters, $RCS$ increases rapidly. After that, from 200 to about 1900 meters $RCS$ is high and decreases at a constant rate. In a small region between 1900 and 2100 meters there is a sharp decrease in $RCS$. Finally, $RCS$ above 2100 is relatively low and decreases again at a constant rate.

The sharp increase in $RCS$ near the ground is due to the incomplete overlap of the FOV of the receiving telescope and the emitted laser beam. This aspect is represented by $C_S$ in the lidar equation. After this maximum at 200 meters, the decrease in $RCS$ is due to the attenuation of the signal by scattering on the aerosol rich air in the ML. In terms of the lidar equation, the contribution of $\beta$ is constant as the aerosols are well-mixed throughout the ML, the decrease in $RCS$ is caused by the term $T^2$. The sharp decrease in $RCS$ around 2000 meter is due to the fact that the composition of the air changes. A transition is made from the ML air with high aerosol concentrations to the FA with low aerosol concentrations. As a consequence, the intensity of the backscattered signal decreases. In the lidar equation this is represented by the backscattering coefficient $\beta$, which is proportional to aerosol concentration and decreases in value going from the ML to the FA. Above this sharp decrease, the low aerosol concentrations cause low backscatter and thus, $RCS$ there is low and also slowly decreases due to (mainly molecular) attenuation.

To get some insight in how different phenomena of the atmosphere are registered by lidar, examples of a full day of lidar measurements are shown in figure 2.4 and 2.5. Figure 2.4 illustrates an almost clear sky day, with considerable convection during the day. Different structures are revealed by the aerosol distribution; especially during nighttime.

At 7 UTC, more than 3 hours after sunrise, the onset of the development of a ML can be distinguished. This layer is characterized by high backscatter as aerosols are mixed into this layer from sources at surface. The growth of the ML continues till an altitude of 1500 meters is reached at 11 UTC. As the ML grows, the distinction between the ML and the air above becomes less clear, because the lidar signal travels through a deeper layer and attenuation of the signal by the aerosols in the ML decreases the signal. This makes the gradient related to MLH less clear.

After growth of the ML in the morning, MLH fluctuates around 1500 m until 14 UTC. After 16 UTC, the lidar signal no longer has the typical vertical profile as described in figure 2.2. Instead, multiple regions of high backscatter are present. The first layer reaches from the ground to an altitude of 500 meter and a second layer of high backscatter is located between 700 and 1000 meters. In between is a layer with lower backscatter. Only the lowest layer is associated with the ML. The second layer is classified as residual layer. The backscatter signal is of the same magnitude as in the first layer as it

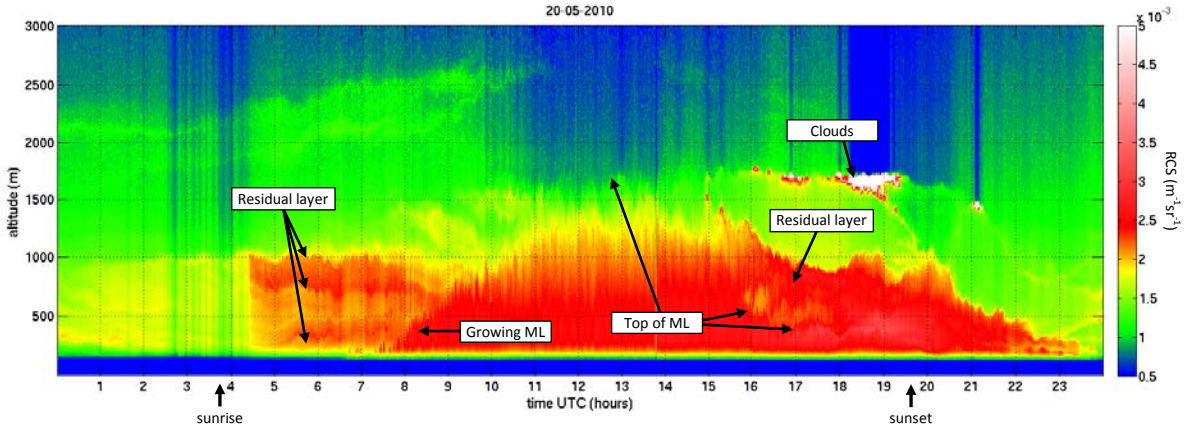


**Figure 2.4.** ***Overview of $RCS$ measured by the ALS450 355nm UV-lidar at Cabauw during a spring-time clear sky day: 20 may 2010. The time of sunrise is 3.39 UTC (5.39 LT), sunset 19.35 UTC (21.35 LT).***

contains aerosols that have been lifted to this altitude earlier that day, but it is no longer in contact with the surface. The only clouds on this day are observed around 1600 meters between 16 and 19 UTC).

A SBL is present during the first 7 hours of this day. This layer does not extend to the lowest altitude where the lidar can measure. Based on the lidar observations, the height of the SBL cannot be determined exactly but it can be assumed to be lower than 200 meters. During these first 7 hours, the backscatter observed in the lowest 1000 meters is higher than above this altitude. This is the residual layer, containing air brought to that altitude by the ML of the previous day. Between 5 and 7 UTC, shallow, slowly undulating layers are visible. Together they form the residual layer and are evidence of a stable stratification.

In contrast to the clear sky day, figure 2.5 illustrates a day with different types of clouds, both related and not related to the boundary layer. The presence of clouds can complicate the interpretation of lidar measurements. On the other hand, clouds can also guide detection of MLH as they can form on top of the ML. Similar to the clear sky day, backscatter in the ML is higher than the air above. The height of the ML on this day is around 1100 meters during daytime. The patches of high backscatter (shown in white) on top of the ML are cumulus clouds and are part of the ML. Above these clouds, the backscatter signal is very weak as it is almost completely attenuated within the clouds. Whatever might be happening above the cloud cannot be detected.

The other patches of high backscatter between 10 and 15 UTC, located between 1500 and 2500 meters are also clouds, but these are not part of the boundary layer and are formed by other processes than convection from the ground. The cloud structure observed between 2 and 9 UTC is the rising cloud base of a cold front that passed the previous day. Another feature is the rain falling out of the clouds of the cold front. It evaporates before reaching the ground. At 12 and 23 UTC stretches of relatively high backscatter extend from the cloud to the surface. These events are rainshowers, although not very heavy ones as the lidar can still see through them.

The left panel of figure 2.6 shows measurement during a fog event. During this morning, the occurrence of fog was reported at Cabauw between 1 and 8 UTC, with the lowest horizontal visibilities of 100-200 m between 5 and 8 UTC. In the course of this period a decrease in the backscatter intensity measured by the lidar is also observed over the entire vertical column. Due to the high optical thickness of the fog, it is hard for the lidar signal to penetrate the layer and measure the aerosol concentrations above.

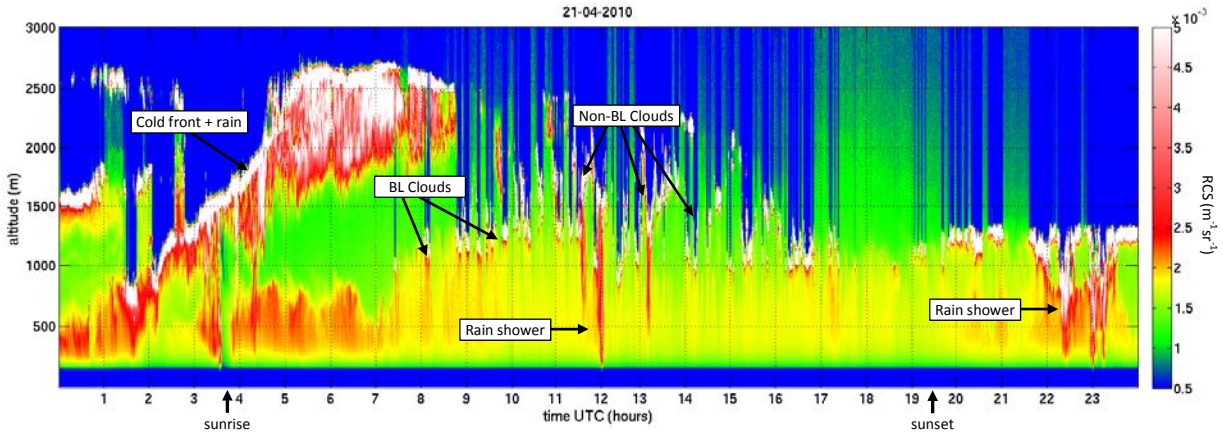


**Figure 2.5.** ***Overview of the backscatter measured by the LEOSPHERE ALS450 355nm UV-lidar during a spring-time heavily clouded day: 21 April 2010.***

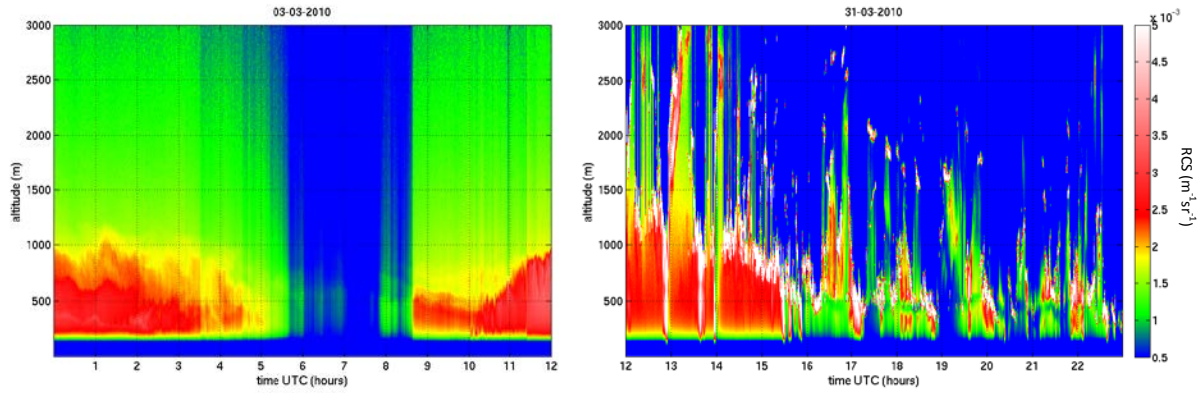


***Figure 2.6. Examples of measured lidar backscatter during fog (left) observed on 3 March 2010 and rain showers (right) observed on 31 March 2010.***

In the right panel of figure 2.6, the afternoon of a day with deep convection and rainshowers is shown. Between 12 and 15 UTC, a few rainshowers occurred but the ML topped by shallow clouds can still be distinguished. After 15 UTC however, there is too much rain for the lidar to be useful for measuring the ML. After a heavy rainshower at 17 UTC it can also be seen that the signal intensity is lower than usual. This is due to water that remains on top of the lidar instrument for some time and attenuates most of the lidar signal. As the water has to evaporate again, the signal only slowly comes back.

Although the aerosol concentrations in the ML are higher than in the FA and aerosol concentrations can be used to detect MLH, interfering features like residual layers of aerosol and rain make the detection of gradient in lidar backscatter associated with the MLH a non-trivial task. Also, fog and rain of top of the lidar instrument attenuate most of the laser beam making the signal too weak to be useful for detection of the MLH. However, several methods exist to circumvent most of these problems to calculate MLH estimates with high spatial and temporal resolution.

## 2.2. Radiosonde

The atmospheric radiosonde is an instrument to retrieve measurements from surface to tropopause. Attached to a balloon it is launched from the surface and during its ascent it measures quantities as temperature, humidity and indirectly wind velocity by tracking the position of the sonde. Usually this is done a few times per minute during the time the sonde is airborne. The vertical profiles produced by the radiosondes are mainly used to give information on the stability of the atmosphere.

Several methods exist to calculate MLH from the radiosonde measurements, including the parcel method (Holzworth, 1964), lapse rate method (e.g. Hayden et al., 1997) and Richardson bulk method (e.g. Vogelezang and Holtslag, 1996).

The parcel method (Holzworth, 1964) is an abbreviation of dry parcel intersection method. It calculates MLH as the intersection of the adiabatic lapse rate with the actual temperature profile. As such, this technique can only be applied on situations in which the atmosphere is unstable. A fictional air parcel is released from the ground and purely lifted by buoyancy. Assuming no mixing with the ambient temperature it keeps rising until reaching an altitude with the same virtual potential temperature. Because correlation with other methods were not as strong as one might expect, addition of a surface excess temperature was proposed by several studies. But whether such a correction improves the results is debateable (Seibert et al., 2000).

The Richardson bulk method is based on the bulk Richardson number $Ri_B$, calculated as

$$Ri_B = \frac{g(z - z_0)}{\theta_v} \frac{\theta_v - \theta_{v,0}}{(u - u_0)^2 + (v - v_0)^2}. \quad (2.4)$$

In this expression, $g$ is the gravitational constant, $z$ the distance from the surface, $\theta_v$ virtual potential temperature and $u$ and $v$ the wind velocity in resp. zonal and meriodional direction. The subscript $0$ denotes the measurement of a quantity closest to the surface.

The term $\theta_v - \theta_{v,0}$ represents buoyancy whereas $(u - u_0)^2 + (v - v_0)^2$ represents shear, the two mechanisms producing turbulence. In unstable situations $Ri_B$ is always negative, because $\theta_v < \theta_{v,0}$ and the wind shear is always positive as it only contains squared values. This makes negative values for $Ri_B$ an indication for turbulence. Under stable conditions, $Ri_B$ is positive because $\theta_v > \theta_{v,0}$. In these situations, buoyancy suppresses turbulence and it depends on the wind shear whether or not turbulence exists. The higher the wind shear, the lower the absolute value of $Ri_B$, so under a certain threshold $Ri_C$ it is assumed there is still turbulence despite the absence of convective instability. A commonly used value is $Ri_C = 0.25$ (Vogelezang and Holtslag, 1996; Zilitinkevich and Baklanov, 2002; Steeneveld et al., 2007).

The lapse rate method is based on vertical gradients of quantities such as water vapour and temperature. As these values are relatively constant in the ML and differ from the values in the FA, gradients in the ML are small but the transition into the FA is marked by a substantial gradient. Hayden et al. (1997) use a threshold of 2 K/km in the gradient of the potential temperature to mark MLH.

## 2.3. Wind profiler

The windprofiler/RASS (Radio Acoustic Sounding System) is a clear-air radar measuring Doppler shift to collect information on the vertical wind profile. For this, a frequency is used between 40 and 1400 MHz. The profiler at Cabauw operates at 1290 MHz. To measure the wind profile it executes a measuring cycle consisting of measurements in four different oblique directions (15.5° off-zenith) and one in the vertical. Combining the measurements from the different directions horizontal and

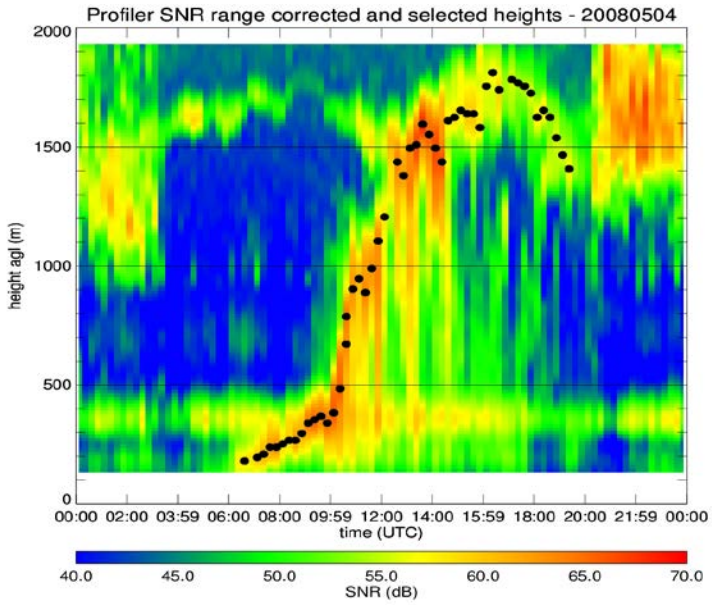


***Figure 2.8. Example of a complete day of wind profiler data. The measurements are averaged on 10-min intervals. The MLH estimates,displayed as black dots, are retrieved by the algorithm described in the text and checked manually afterwards.***

vertical wind speed can be determined. For each direction a low and high mode are available. The low mode as a resolution of 60 m and measures from an altitude of 100 to 2000 m. The high mode has a resolution of 200 m and measures from 600 to 7000 m. The intensity of the returning signal primarily depends on inhomogeneities in the atmospheric moisture and temperature caused by turbulence. The signal-to-noise ratio (SNR) is directly proportional to these inhomogeneities, captured in the refractive index structure function $C_n^2$ (e.g. Ottersten, 1969). Due to the entrainment at the MLH, $C_n^2$ exhibits a (local) maximum at this height. The method used to derive MLH from windprofiler measurements is based on this characteristic.

Next to the SNR, the width of the Doppler spectrum is also used to determine MLH. The spectral width is related to the differences in wind speed in the probed volumes. This width is smaller in the entrainment layer than in the mixing layer itself and also increases again into the free atmosphere. So, in contrast with $C_n^2$, MLH is associated with a minimum in spectral width.

The procedure to estimate MLH based on the method described by Angevine et al. (1994) only uses the measurements from the oblique directions. From the four different profiles the median is retrieved every 10 to 20 minutes. A spline is interpolated to create a more smooth profile with an enhanced vertical resolution of four times the original resolution, 15m for the low mode and 50m for the high mode. From this interpolation, all local maxima are listed. Basically, the highest maximum corresponds to MLH, but the selection is guided by the width. From this list the altitude most likely to respond to MLH is selected, based width of the Doppler spectrum and a comparison against local maxima from previous and next time steps.

## 2.4. Instruments used in this research

The main instrument used in this research is the LEOSPHERE ALS450 UV-lidar located at the Cabauw Experimental Site for Atmospheric Research (CESAR). This lidar measures at a wavelength of 355nm. Data is recorded with a temporal resolution of 30 s and a vertical resolution of 15 m. This lidar operated for short periods in 2007-2009. From 2010 on, a more continuous dataset exists with data available on average 270 days per year. Usually, lidars have either continuous datasets (ceilometers and lidars used in operational networks) or high quality measurements (experimental lidars). Because the ALS450 lidar has both long timeseries and good quality it is ideal for this research. An overview of the specifics of this lidar is given in table 2.2.

To test the new method and to get a quantitative measurement of its performance, a comparison is made with MLH estimates from other instruments. Observations for this are taken during a 12 day-period in May 2008, part of the EUCAARI IMPACT campaign at Cabauw. This was a collaboration of several European institutes from the Netherlands, France, Germany, Poland and Finland. The objective of this campaign was to quantify the indirect aerosol effect. During the campaign simultaneous observations of the boundary layer were made by many different instruments. These

| **Parameter/specification** | **value** |
|---|---|
| *Lidar specifications* | |
| **Transmitted wavelength** | 355 nm |
| **Pulse repetition frequency** | 20 Hz |
| **Pulse energy** | 12 mJ |
| **Pulse duration** | 6 ns |
| **Telescope diameter** | 20 cm |
| **Time resolution** | 30 s |
| **Height resolution** | 15 m |

***Table 2.2. Overview of specifications of the LEOSPHERE ALS450 UV-Lidar.***

included remote sensing instruments like lidar, radar, radiosonde, scintillometer and total sky imagers. But also temperature, wind, flux and aerosol measurements at the ground and in the Cabauw measurement tower. Even helicopter and airplanes flights were performed to measure cloud droplet spectra and aerosol concentrations in the air. Of these observations, radiosonde, wind profiler and lidar measurements are included in our comparison.

# 3. EXISTING LIDAR MLH DETECTION METHODS

Manual assessment of lidar measurements is still one of the most powerful tools to identity MLH throughout the day. With knowledge on what influences the mixing layer (e.g. time of sunrise and sunset or presence and type of clouds), the larger structure of regions corresponding to the ML, residual layers and FA can be recognized. This structure can then be used to estimate the exact evolution of MLH. By judging the overall structure and local differences iteratively, it can be distinguished whether an individual gradient is part of a larger structure or noise. The human brain is very good at this sort of pattern recognition, which makes it an excellent instrument for tracking the evolution of MLH.

The iterative character of finding the MLH is difficult to compile in a set of rules within a computer algorithm. With constantly changing values of the backscatter profile, fixed thresholds cannot be used and all measurements have to be processed relatively to each other.

The most commonly used techniques applied to lidar measurements are the gradient method (Flamant et al., 1997 or Menut et al., 1999), variance analysis (Hooper and Eloranta, 1986 or Menut et al., 1999) and continuous wavelet transforms (Haij et al., 2007). Other techniques tried in previous research are fitting idealized backscatter profiles (e.g. Steyn et al., 1999 or Eresmaa et al., 2006) or Canny edge detection (Morille et al. 2007). To be better able to judge the algorithm proposed in this research a short explanation of the mentioned techniques is given below.

## 3.1. Gradient method

Algorithms (e.g. Flamant et al., 1997; Menut et al., 1999) based on the gradient method are based on the simple reasoning that the ML is characterized by high aerosol concentrations and the FA by low aerosol concentrations. Because these two air masses hardly mix, the interface between them is marked by a rapid decrease in backscatter intensity. This decrease in backscatter can be found by calculating the vertical gradient. Assuming a nearly constant aerosol concentration in the boundary layer and a low aerosol concentration in the free atmosphere, the maximum of the vertical gradient will coincide with the MLH. An example is shown in figure 3.1. Variations of this technique are the calculation of the second derivative (infliction point) or the derivative of the logarithm of the backscatter signal.

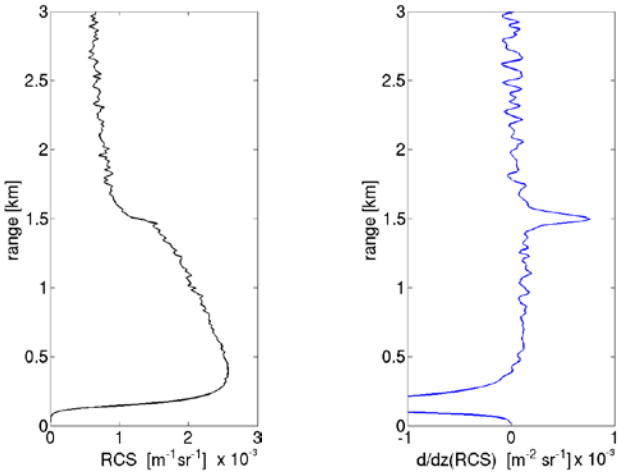


***Figure 3.1. Example of the gradient method. Left) Vertical profile of RCS on 20 May 2010, 12 UTC. right) Corresponding vertical gradient. By calculating the vertical gradient in RCS, the MLH appears as a local maximum.***

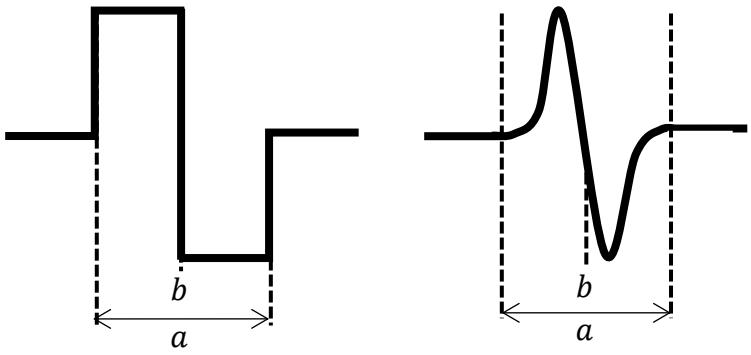


***Figure 3.2. Examples of the Haar and Gaussian first derivative wavelet. The parameters for dilation $a$ and position $b$ are shown schematically.***

## 3.2. Wavelet covariance transform (WCT) method

The basis of the WCT method is the same as the gradient method. By examining the vertical structure of the aerosol concentration the MLH is identified. But in this method the technique used to find the MLH is more complex than calculating a vertical derivative. Instead, the covariance between the lidar signal and a prescribed wavelet is calculated, this wavelet should resemble the optimal. Commonly used wavelets resemble the shape of the ML with a sudden decrease in value to mimic the decrease in backscatter associated with the MLH. Examples are the Haar wavelet (e.g. Haij et al. 2006; Baars et al, 2008) or the first derivative of the Gaussian wavelet (Morille et al. 2007).

The covariance transform is calculated as

$$W(a,b) = \frac{1}{a}\sum_{r} P(r,t)\cdot h\left(\frac{r-b}{a}\right) \tag{3.1}$$

Where $P(r,t)$ is the range-corrected lidar backscatter signal, $r$ the measurement height and $h$ the wavelet used to compare with. For $h$, the dilation $a$ determines the width of the wavelet and $b$ is the altitude around which the wavelet is centered.

By calculating the transform for different altitudes $b$, the covariance between the wavelet and signal changes. Because the wavelet resembles the shape of the backscatter, the covariance increases if the center of the wavelet is aligned with the decrease in backscatter at MLH. Consequently, the covariance will display a local maximum at the altitude of the MLH. By increasing (decreasing) the size of the wavelet with parameter $a$, the transform will be more sensitive to large (small) structures.

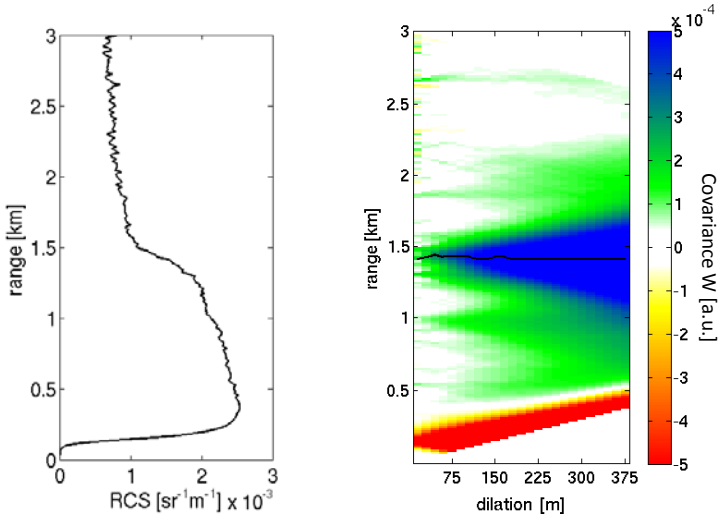


***Figure 3.3. Example of the WCT method. Left) Vertical profile of lidar backscatter on 20 May 2010, 12 UTC. Right) Calculated WCT for different dilations and altitudes, using the Haar-wavelet. The maximum covariance is indicated by the black line and corresponds well to the sharp decrease in backscatter at MLH.***

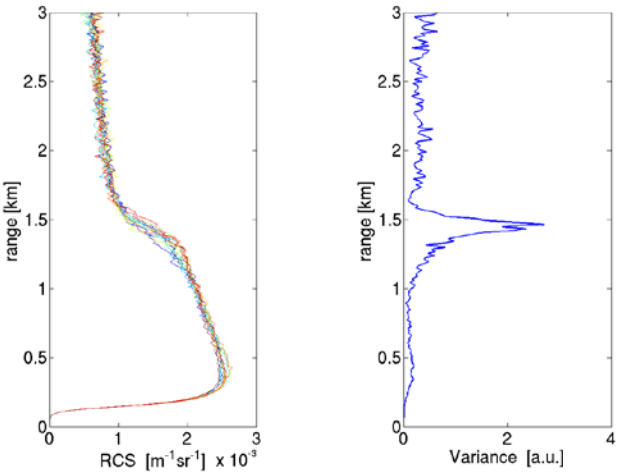


***Figure 3.4. Example of the variance method. Left) Vertical profile of RCS on 20 May 2010, 12 UTC. Right) Variance of the RCS during one hour. The maximum in variance corresponds well with the sharp decrease in RCS at MLH.***

For small dilations, the wavelet transform will be influenced by noise, as it is a small scale feature. For large dilations, the transform is more robust, but also less exact in determining the location of the MLH. Next to that, large wavelets can capture different structures like clouds or the residual layer together with the MLH. The optimal value for parameter $a$ is equal to the depth of the entrainment zone, which is not known beforehand (Brooks, 2003). To circumvent this problem, an optimized fixed or height-dependent dilation can be used (e.g. Baars et al., 2008) as well as an average of 24 different transforms using dilations (Haij et al., 2007). Morille et al. (2007) track the local maxima in the vertical along decreasing dilation to pinpoint the exact location of the MLH.

## 3.3. Variance method

Algorithms (e.g. Hooper and Eloranta, 1986; Piironen and Eloranta, 1995; Menut et al, 1999) based on the variance method compare data in the temporal domain instead of the vertical domain. As mixing of the air in a CBL is caused by individual rising thermals, succession of rising polluted ML air in thermals and clean FA air in between leads to large variations in backscatter intensity. Furthermore, the entrainment of FA air by small eddies at the side of thermals leads to even more variations, although on a much smaller (spatial and temporal) scale.

By calculating deviations from the mean backscatter within a certain period (e.g. 1 hour) the mixing layer height can be distinguished. This is done in a similar way as one would calculate variance, hence the name of this method.

A large disadvantage of this method is the low temporal resolution inherent to the technique. Due to the need of averaging, an estimate for MLH cannot be produced for every timestep and details on short timescales will be lost.

## 3.4. STRAT2D method

This method, first described in Morille et al. (2007) and further developed in Haeffelin et al. (2010) has been presented as a method to be applied broadly to different kinds of lidars. Also, the code of this method has been made available in open source to encourage others to use it. For MLH detection it uses an algorithm called Canny edge detection, which is a 2D pattern recognition algorithm designed to extract edges from a picture. Here it is used to trace the boundary between ML and FA. This method is explained below because the new algorithm proposed in this research is compared against STRAT2D.

The first step in this method is to calculate horizontal (time) and vertical derivatives for every single measurement point. This can be done by using a simple central differences scheme, but the STRAT algorithm uses the convolution matrices of the Sobel operator. For every measurement point a value

is calculated using the neighboring measurement points in the spatial as well as the temporal domain. So not only the measurements above and below the considered measurement point are taken into account, but also the measurements of subsequent timesteps. Two convolution matrices are constructed in such a way that every neighboring pixel has the same weight when these gradients are added up. For the horizontal gradient we have

$$G_x = \begin{bmatrix} -1 & 0 & +1 \\ -2 & 0 & +2 \\ -1 & 0 & +1 \end{bmatrix} \cdot P \tag{3.2}$$

For the vertical gradient we have

$$G_y = \begin{bmatrix} +1 & +2 & +1 \\ 0 & 0 & 0 \\ -1 & -2 & -1 \end{bmatrix} \cdot P \tag{3.3}$$

From these, the magnitude $G$ and direction θ of the total gradient are calculated as:

$$G = \sqrt{G_x^2 + G_y^2}, \qquad \theta = atan2(G_x, G_y) \tag{3.4) \& (3.5}$$

Because the measurements are on a rectangular grid, θ is simplified to the closest of the following 4 directions: 0°, 45°, 90° and 135°. Of these directions, 0° indicates gradients pointing to the north or south (vertical) direction, 90° for gradients to the east or west (horizontal) direction. In between are the 45° direction for gradients pointing north-east or south-west and the 135° direction for gradients in the south-east or north-west direction. As an example, gradients with 22,5° $<$ θ $\leq$ 67,5° or 202,5° $<$ θ $\leq$ 247,5° are labeled as 45°. A complete overview is given in figure 3.5.

In the next step, the actual edges are constructed. For every pixel, the direction is now grouped into one of the 4 general directions. To determine whether the pixel should be marked as an edge, the magnitude $G$ of the gradient is compared to the magnitudes $G$ of the 2 neighboring pixels along this direction. If the pixel has the highest value, it is marked as an edge, if not, it is rejected. This way, gradual changes are brought down to an edge of a single pixel.

To come to a final image containing only the strongest gradients, double thresholding (also called hysteresis thresholding) is used. First, all edge pixels above a certain threshold are selected. These pixels are permanently selected as edges. Now, a second, lower threshold is used. Any pixels connected to the high threshold pixels, below the first threshold, but above the second threshold are also selected as permanent edge. This way, an edge slowly fading away or weak parts of an edge can still be traced.

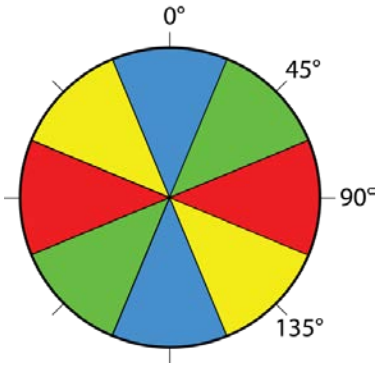


***Figure 3.5. Overview of the directions simplified to one of the 4 general directions. Any direction shown in blue is labelled as 0°, green as 45°, red as 90° and yellow as 135°.***

The STRAT algorithm continues to select three candidates for MLH every timestep. This is done by finding the edge with the lowest altitude and the edges with the highest and second highest magnitude $G$. From these candidates, the strongest gradient is preferred, provided it has a backscatter ratio $B$ lower than 0.9. This implies that the selected altitude indeed marks the MLH and it is not an erroneous, noise induced gradient. $B$ is calculated as the ratio between the average of 3 measurements 90 meters above the edge and the average of 90 meters below the edge:

$$B(r,t) = \frac{\sum_{i=-1,0,+1} RCS(r + 90 + i\Delta r, t)}{\sum_{i=-1,0,+1} RCS(r - 90 + i\Delta r, t)} \tag{3.6}$$

If $B$ is higher than 0.9, the strongest gradient is rejected as MLH and the 2nd strongest gradient is considered. For this gradient the ratio $B$ is also calculated. If this gradient gets rejected as well, the same procedure is done for the lowest gradient. If $B$ is too low for this last gradient, the presence of a cloud within a prescribed range is checked. If there is a cloud, the cloud base is considered to be the MLH. If there are no clouds, no MLH is given for that timestep.

## 3.5. Common difficulties

The examples in figures 3.1, 3.3 and 3.4 showed a boundary layer with a simple structure and detection of MLH straightforward. Unfortunately, the boundary layer usually has a more complex structure. Different features like a residual layer or advected layers of polluted air can cause multiple strong gradients in the backscatter profile, disturbing the detection of MLH. These additional gradients can be stronger than the gradient related to the MLH. Therefore, a maximum in the vertical gradient cannot be marked as MLH automatically. Because the ML extends from the ground up, one could argue that all these other layers and structures always occur above the ML and that the gradient closest to the surface coincides with the MLH. However, the ML is never perfectly mixed and additional gradients can occur within the ML. Usually these irregularities are small, but they can interfere with detection of the right maximum in cases where the gradient at the MLH is not very well pronounced, e.g. with low aerosol concentrations in the ML, the gradient at the interface with the FA can become small.

A common feature of the MLH detection methods discussed above is that MLH is estimated for each timestep individually. Even the STRAT algorithm, although the Canny edge detection is 2D, the final selection process estimates MLH independent of adjacent timesteps. This can lead to solutions with large jumps in MLH between timesteps. This typically happens during the morning transition, with a residual layer present above the ML. Usually strong gradients occur at the MLH at the beginning of the day when the ML is still shallow, because the pollution is spread over relatively small volume. As the ML increases in depth, this volume increases and the aerosol concentration in the ML decreases. Consequently, the gradient at the MLH becomes weaker. When the strength of the gradient at the MLH decreases to a level under the strength of a residual gradient, the MLH estimate can instantaneously jump from the MLH to the residual layer. However, MLH is a relatively slowly evolving quantity. Common growth rates are between 100 and 400 m/h and large jumps should be rejected a priori. By processing information from both the temporal and spatial domain simultaneously, the difference between timesteps can be limited. This could improve the selection of the right gradient as MLH.

The continuous and slowly evolving character of the MLH and simultaneous evaluation of timesteps is the foundation of proposed 'Pathfinder' method. In order to do so, it applies graph theory and Dijkstra's algorithm (1959). A short introduction of graph theory and Dijkstra's algorithm is given in section 1.2. The details of the new method are discussed in chapter 4.

# 4. PATHFINDER METHOD

The Pathfinder method estimates MLH by finding a connected series of MLH estimates containing as much strong gradients as possible. The main input of the algorithm is a matrix containing the range corrected backscatter (RCS) for one day. From this signal a field of vertical gradients is computed. This gradient field is translated into a graph and MLH is calculated for the daylight period using Dijkstra's shortest path algorithm. To guide determination of the MLH, several restrictions are calculated from both the signal and gradient field itself. When the estimates for MLH are derived, a ratio of backscatter intensity between the signal above and below MLH is calculated as a quality flag. Together with information on precipitation and fog, this serves as an indication of the reliability of the MLH estimates. A detailed description of the consecutive steps of the algorithm is given in this chapter.

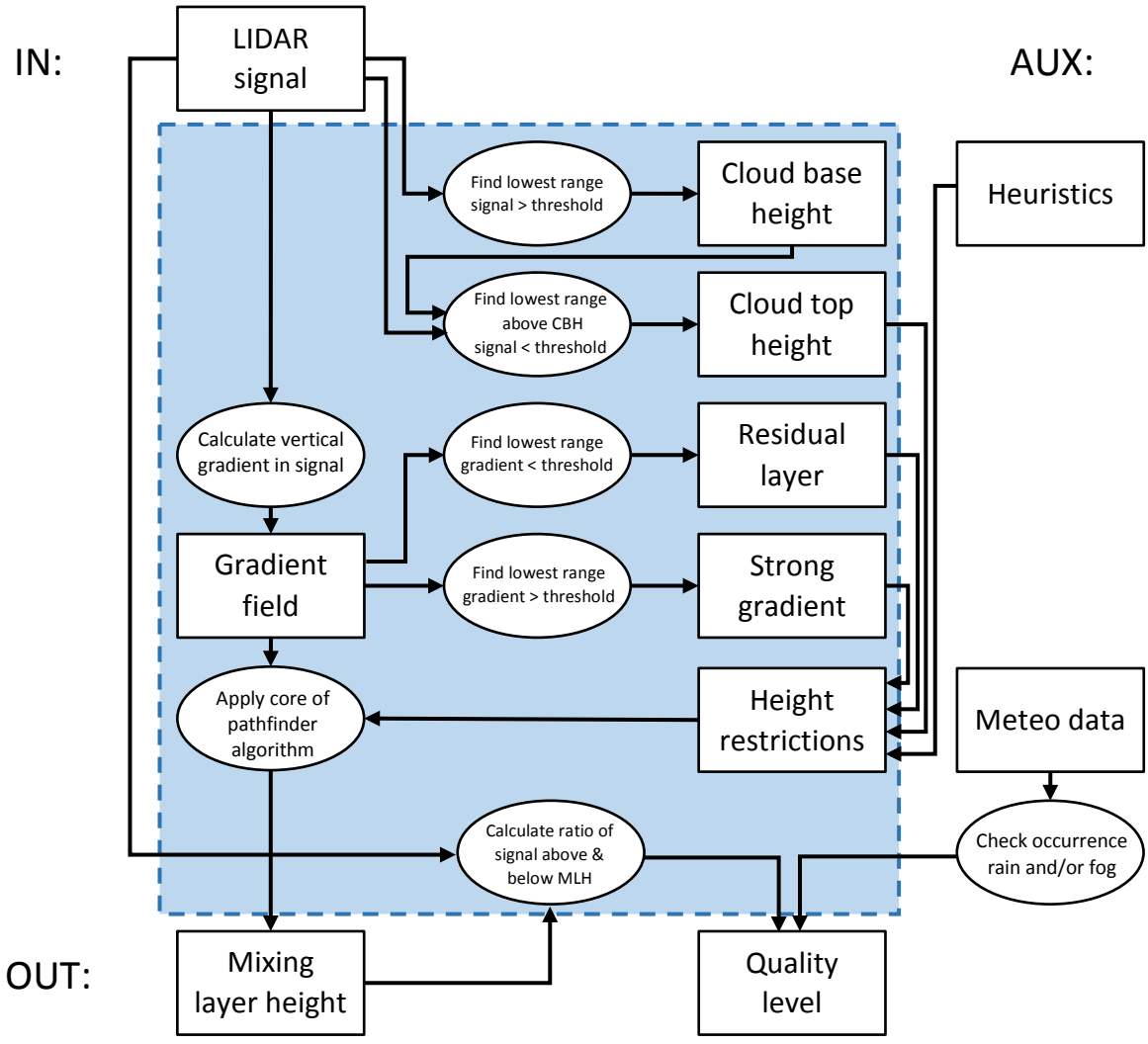


***Figure 4.1. Schematic overview of the complete Pathfinder algorithm. Internal operations and variables are grouped within the blue area.***

## 4.1. Gaussian smoothing

The starting point of the algorithm is a matrix containing RCS. Because the algorithm works with the values of vertical gradients between individual data points it is important to reduce the influence of noise. Gradients caused by noise can trigger erroneous estimates of MLH and reduce the performance of the method. To counter the influence of noise, the first step in the algorithm is to smooth the RCS data. This reduces the influence of a noise and leads to a more stable solution of the algorithm. However, gradients are also smoothed out and the estimates of MLH will become less accurate.

The method used for smoothing is a Gaussian smoothing filter. The new value of each value is a weighted average of that pixel's neighborhood, but the information is scaled using a Gaussian distribution and gives the closest neighbors the largest weight:

$$g(t,r) = \frac{1}{2\pi\sigma^2} e^{-\frac{(t-t_0)^2+(r-r_0)^2}{2\sigma^2}} \tag{4.1}$$

The indices $t$ and $r$ specify timestep and range respectively. The subscript $0$ indicates the time and range of the measurement point being smoothed. The width for this distribution has to be chosen beforehand. Wiegner et al. (2006) argue that a value most optimal for lidar measurements is 37.5m FWHM (full width at half maximum), which corresponds to $\sigma = 15.92$ m. From a strictly mathematical point of view, the whole backscatter matrix has to be taken into account to smooth a single value, because the values of the Gaussian do not decay to zero for $\pm\infty$. But the error introduced by truncating after multiple standard deviations in each direction is negligible. Here the value of $5\sigma$ is chosen and measurement points outside the vertical range of 79,6 m are neglected.

## 4.2. Gradient field

The next step in the algorithm is to construct a field of vertical gradients $G$ from the range corrected backscatter RCS. These gradients are computed as

$$G(t,r) = \frac{RCS(t,r+1) - RCS(t,r-1)}{2\Delta z}. \tag{4.2}$$

Where the indices $t$ and $r$ are similar to the previous equation and $\Delta z$ is the vertical resolution of the measurements Because the focus lies on negative gradients associated with the MLH, strong or weak negative gradients will be referred to as simply strong or weak gradients. Positive gradients will be mentioned explicitly.

Several features can be observed in the gradient field, shown in figure 4.2. First there is the large band of strong gradients related to MLH during the day. This gradient starts to appear near the surface around 7 UTC and rises slowly until around 12 UTC. After that, it decreases slowly to disappear again near the surface at 18 UTC. Characteristic for this gradient are its gaps and irregular shape caused by the discontinuous nature of the individual thermals causing the mixing in the ML. Next to the gradients associated with the MLH, several narrower bands of high (positive and negative) gradients can be seen. The well pronounced gradients between 250 and 1000m before 7 UTC are linked to the residual layer. The same can be observed between 16 and 20 UTC at up to about 1000 m where mixing by convection has ceased and a new residual layer has formed.

As shown in the figure, even a day with clear skies has multiple structures and gradients making the tracking difficult. Especially during the morning and evening transitions, when other gradients are in the same altitude range as the MLH. Also, it is not unusual to find a stronger gradient on top of the residual layer than on the ML.

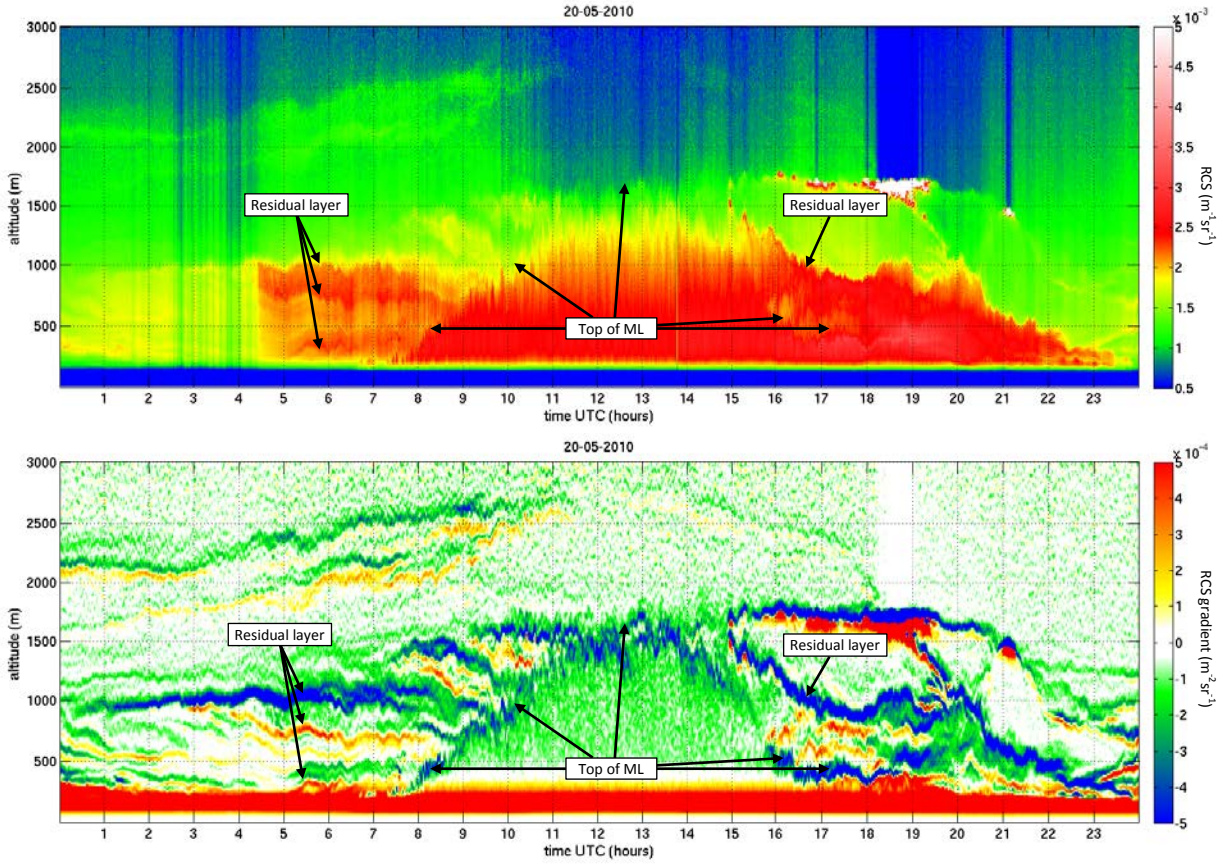


***Figure 4.2. (top) RCS measured by the ALS450 355 nm UV-lidar at Cabauw. Data have been smoothed as described in the text and (bottom) gradient field computed from the RCS. Negative vertical gradients are represented by positive values and shown in green and blue. Positive gradients are represented by negative values and shown in yellow and red.***

## 4.3. Guiding restrictions

Although the mixing layer can exhibit a lot of different features, some structures are the same for all types of mixing layers. Identifying clouds and residual or advected aerosol layers can support to separate the ML from the FA and are used to guide the algorithm to search for MLH. Because the ML is a phenomenon extending from the ground up, the guiding structures will provide a maximum height for the MLH.

*Clouds*

The presence of clouds, in particular cumulus and stratocumulus, can reveal the structure of the atmosphere and the boundary layer. Although there are numerous other types of clouds and many mechanisms responsible for their formation, clouds only form above or on top of the boundary layer. Even though the ML can be lower than the clouds, it will never extend above a cloud layer. Based on this, if clouds are present, the maximum height of the MLH is restricted to the top of the first cloud base. Different situations and set-ups in cloudy boundary layers are described in section 2.1.3.

Cloud detection in the Pathfinder method is based on the strength of the backscatter, which is possible due to the relatively high backscatter on cloud droplets compared to aerosols. For each timestep, the lowest altitude at which the backscatter exceeds a certain threshold is marked as cloud base height (CBH). After that, the lowest altitude above the CBH at which the backscatter drops below the threshold is marked as cloud top height (CTH). With the identification of the lowest cloud layer, the area above the CTH can be excluded from the search for MLH. To ensure inclusion of boundary layer cloud a margin of 75m above CTH is applied.

One of the difficulties of this procedure can be high aerosol concentrations for which backscatter might exceed the threshold for cloud detection. Although this rarely occurs, a certain altitude within the mixing layer will then be marked as CBH and the real MLH might be excluded from the searching range. Another problem is the possible total extinction of the lidar signal before it reaches CTH. If this is the case, clouds appear shallower than they actually are and the detected CTH is too low. It is difficult to assess whether the signal penetrates the complete cloud or not. Nevertheless, the detected CTH will be the best estimate of the cloud top, as this is the highest altitude the lidar receives backscatter from. A third difficulty is high backscatter on raindroplets. As this backscatter is in the same range as cloudroplets, rainshowers are also identified as clouds and the searching range might be restricted under the actual cloud. Although attribution of cloud base might be incorrect, this might not be a problem for MLH detection because the air for the ML does not mix into the downdraft of the rainshower. More details are discussed in section 5.1.3.

In the algorithm, a rough distinction is made between boundary layer and non-boundary layer clouds. As fair weather cumulus and stratocumulus on top of the boundary layer are relatively thin, thickness of the cloud is used to determine whether a cloud is part of the ML or not. For every set of CBH and CTH, the thickness of the cloud is calculated. When this thickness exceeds a value of 500 m, the corresponding cloud is assumed not to be related to the ML. In these situations, the searching range is restricted to the cloud base height instead of cloud top.

*Detection of strong negative gradient*

The detection of MLH in this algorithm is based on finding the vertical gradient in backscatter associated with it. Even though this gradient can be weak or even absent at times, a strong gradient is always an indication of a separation between air masses. In case of multiple strong gradients, the searching range can be restricted to the altitude lowest gradient. Because the ML is a phenomenon that extends from the ground up, mixing from the ground stops at that height and MLH is not located at a higher altitude.

For the detection of a strong negative gradient the lowest altitude at which the (negative) vertical gradient is stronger than a certain threshold is marked. Similar to the cloud restriction, measurements higher than 75m above the restriction are excluded.

Difficulties with restricting search range based on strong gradients are inhomogeneities within the ML. These mainly occur during daytime and are linked to the structure of the rising thermals in a CBL. To reduce the influence of these inhomogeneities, without having to smooth the data too much, the restricting altitude is taken as the maximum altitude of a strong gradient found within a time window of 2 minutes around a certain timestep.

Next to that, a threshold sufficiently detecting structures in the morning period also triggers on the inhomogeneities in the ML. On the other hand, a threshold not triggering on the inhomogeneities in the ML misses a lot of the structures in the morning period. To circumvent this, two thresholds are used: one for the morning period before convection and one for the convective period. The convective period is different for each day, but the onset usually takes places between a few hours after sunrise (e.g. Angevine et al. (2001) found a median delay of 2.7 hours after sunrise at Cabauw). In the algorithm, the average of 3 hours is used for the convective delay. The period between sunrise and the convective delay is considered as the morning period and the period after that is the convective period.

*Detection of positive gradients*

With the majority of the aerosol sources situated at the surface the aerosol concentration in the ML is usually higher than in the FA, but the opposite is possible as well. So, similar to negative gradients, positive gradients are an indication of the separation of air masses. Regardless of the sign of the gradient, a gradient can only occur if there is no mixing between the two air masses. Therefore, air above a strong positive gradient cannot be part of the mixing layer. An example of such a situation could be the advection of polluted air from an urban area into a relatively clean environment.

Like the restrictions based on negative gradients, the lowest altitude at which the gradient is higher than a certain threshold is marked. Again, two thresholds are used and the restriction takes into account several consecutive time steps to exclude measurement points more than 75m above the restriction.

The most important difficulty associated with the restrictions based on positive gradients is the presence of clouds. Because of the high reflectance of clouds the backscatter increases sharply at cloud base, causing positive gradients. Following the procedure as described above would mean the area above the cloud base is excluded for MLH while (strato)cumulus clouds can be part of the ML. To prevent exclusion of ML clouds, interaction with the cloud detection is needed. When a cloud base is found within a range of 300 meters above a positive gradient the search range is not restricted on this argument.

An additional difficulty is caused by very thin clouds or clouds that are just about to form. In these situations the backscatter is increased by the few droplets that have formed and a positive gradient is found on that altitude. However, the backscatter intensity is not (yet) high enough to classify as a cloud. In absence of cloud detection, the gradient based restriction erroneously excludes the new cloud from the searching range.

At the lower range of the backscatter profile, a positive gradient always exists because of the incomplete overlap of laser and telescope. The overlap is the same for all timesteps, but the altitude where the gradient becomes negative varies depending on the profile of the backscatter. To prevent a trigger on positive gradients associated with the incomplete overlap, detection starts at the altitude where the gradient switches sign from positive to negative for the first time.

*Heuristics*

From literature and measurements, the extent of the ABL in the mid-latitude is well-known. For example, the mixing layer in Cabauw rarely extends above 750 m during night and 3000 meter during the day. This is implemented into the algorithm by restricting the searching range during the morning period to the night value. After that, a linear increase of 2.5 $ms^{-1}$ is allowed, until the maximum altitude for daytime is reached. For the remainder of the day, the search range is limited by this daytime maximum.

*Summary*

The different restrictions are used to eliminate regions from the ML to exclude interfering gradients for a more reliable MLH estimate with Dijkstra's algorithm. An example of this is shown in figure 4.3. For example, before 8 UTC the restriction based on positive gradients excludes all measurements roughly above 500m. This way, the gradients of the residual layer will not interfere with MLH detection. Although the residual layer is detected as strong gradient, this will not exclude it from the searching range because of the 75m margin. In contrast, the residual layer is excluded by the negative gradient between 17 and 18 UTC because sufficiently strong gradients appear near the surface.

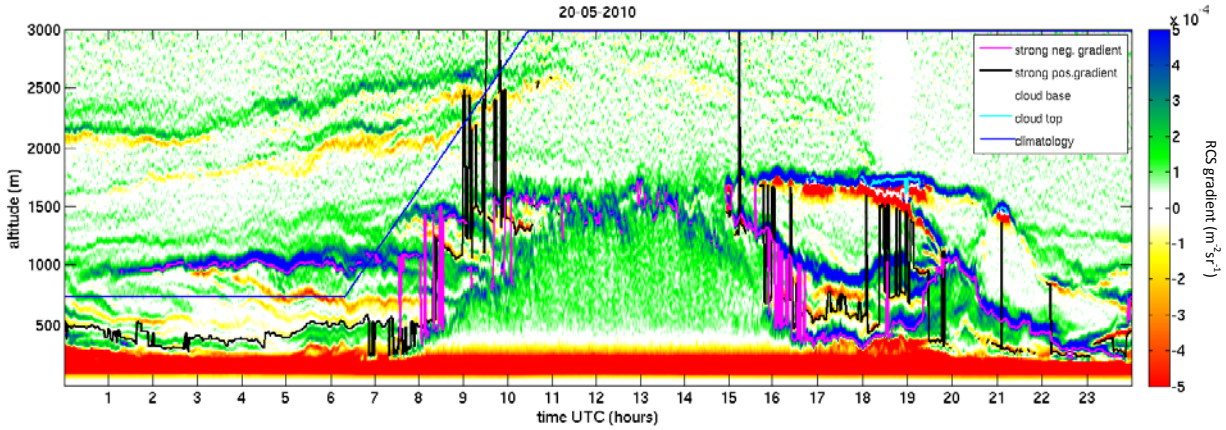


***Figure 4.3. Example of the restrictions to guide the graph based path finding algorithm. The criteria of the restrictions are strong negative gradients (magenta), strong positive gradients (black), cloud top (cyan) and heuristics (blue). All measurement points above at least one of these are excluded as possible MLH.***

## 4.4. Constructing graph

After confining the searching range, the algorithm translates the measurements into a graph. Because the goal is to connect a series of points representing the evolution of the MLH in time, the following procedure ensures any path in the graph represents a physically possible evolution of the MLH.

Basically every point in the gradient field is a vertex in our graph. But not all vertices are connected to each other. Instead, to form a proper series of points representing MLH evolving in time, edges are only drawn between vertices under certain conditions. A schematic overview is shown in figure 4.4. Here, time is on the horizontal axis and altitude is on the vertical axis. The vertices of a single column correspond to the measurements of the different rangegates at a specific timestep and the vertices of a single row correspond to measurements of the same rangegate at different timesteps. The first condition is that only vertices of consecutive timesteps are connected by edges. Connections between vertices of the same timestep (1) or connections between vertices more than one timestep apart (2) are not allowed. Also, a connection going back in time (3) is not allowed. The second condition simulates the continuous character of the MLH. Connections are only allowed within a certain vertical range from the originating vertex. As such, a connection to a vertex outside the vertical range is not allowed (4). After testing a range of values, a maximum growth rate of $2{,}5 ms^{-1}$ was used to restricting the vertical range, e.g. the allowed range is 75m for a timestep of 30s. This allowed tracking of the MLH at the level of individual rising thermals. Together, these conditions ensure connections (5) leading to a path imitating the evolution of the MLH.

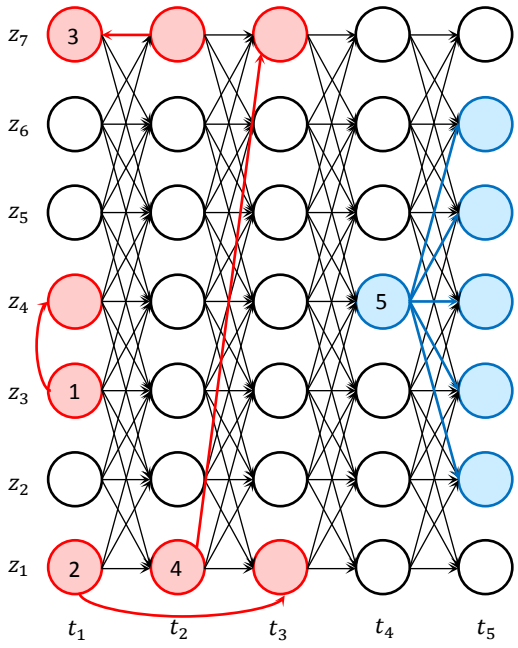


***Figure 4.4. Translation of measurements into a graph. The black arrows represent allowed connections, ruling out the connections shown in red. An example of how a series of vertices could form the evolution of the MLH is shown in blue.***

## 4.5. Adding weights to graph

The procedure to construct graphs does not provide a way to determine which path represents the real MLH. For this, gradient based weights are assigned to the connections in the graph. Connections pointing to a certain vertex get a value corresponding to the point in the gradient field represented by that vertex. The values of the weights $W$ are calculated as:

$$W = -\left(\frac{\partial}{\partial z}\mathrm{RCS}\right)^{-1}. \tag{4.3}$$

Using this conversion, high gradients correspond to low weights and low gradients correspond to high weights. Because Dijkstra's algorithm searches for the path with the lowest total weight, the estimate for MLH will include as much strong gradients as possible. However, with this translation from gradient to weights, positive gradients yield a negative weight. Because negative weights are not allowed in Dijkstra's algorithm these are given a high weight value corresponding to a very weak negative gradient. This ensures that the algorithm only includes these vertices if there is no better option.

## 4.6. Dividing into time windows

Constructing a graph for a full day UV-lidar data would mean that it contains about 576,000 vertices and almost 6 million edges for in the lowest 3 kilometers. Together this leads to an even higher amount of possible paths. Taking into account all measurements of a day at once is too much for a workable algorithm. Therefore, it is needed to split the day into multiple time windows and apply the algorithm to those windows separately. As computational costs determine the upper limit of the window size, the lower limit is determined by the typical scales within the ML. In our algorithm the measurements are grouped into windows of 15 minutes, enough to capture several thermals simultaneously. For each window, an optimal path is calculated from a starting point on the first timestep to one of the allowed vertices of the last timestep of the window. After the calculations of one window are completed, the end-point is transferred and used as starting point for the next window. This is continued until all time windows are processed. By overlapping the first and last timestep of the windows, a connection is made between them and a continuous series MLHs is constructed.

## 4.7. Calculating MLH

After the guiding restrictions are applied, time windows of 15 minutes are created and the measurements are translated into a graph and Dijkstra's algorithm is used to calculate the most probable evolution of the MLH. For the starting vertex in this first time window, the altitude of the strongest negative gradient (taking into account the several guiding restrictions) is used. For all other windows, the last timestep of a previous window is used as the first timestep in the next.

Although an ascend or descend of 2,5 $ms^{-1}$ is allowed between timesteps, the allowed endpoints within a single time window are much more restricted to simulate the slowly evolving character of the MLH. Between the first and last timestep of a time window, MLH may not change faster than 1 $ms^{-1}$. This is more than found in research (e.g. Baars et al. (2008) measured growth rates of 1000 $m\ hr^{-1} = 0.278\ ms^{-1}$ only in extreme cases), but this does not seem to hold for timescales of 15 minutes and implementing lower values caused the algorithm to be unable to track fast morning transitions.

## 4.8. Quality flag

To give an indication of the quality of a MLH estimate a quality flag is calculated. This is not a quantitative measure but a combination of conditions to be used next to the outcome of the algorithm to interpret the reliability of the MLH estimate.

The first condition is based on the ratio of the RCS above and below the estimated MLH, similar to the quality flag used in de Haij et al. (2007) and Morille et al. (2007). Here, this ratio is calculated as the average RCS 150$m$ above MLH divided by the average RCS 150$m$ below MLH. If the algorithm pinpointed the correct MLH, this ratio is small because the backscatter in the FA is lower than in the ML. If the algorithm marked an erroneous, noise induced gradient within the ML or FA, the backscatter above and below the estimate are comparable and the ratio is close to 1. However, if the top of the residual layer is marked as MLH or aerosol concentrations in the ML as low, this ratio can also be small. Consequently, a high ratio is an indication of an incorrect MLH estimate, but a small ratio is no guarantee the MLH is correct. As a threshold, ratios above 0.9 are considered an indication of an incorrect MLH estimate.

Two other conditions are based on surface meteorology. As explained in section 3.1 fog and rain can disrupt the lidar measurements and therefor reliable estimate of MLH. Whenever the rain occurred or the vertical visibility is below 200 m, these timesteps are marked as possibly incorrect MLH estimates.

# 5. RESULTS

As explained in chapter 4, the algorithm has several tuning parameters like the thresholds for the guiding restrictions, window size and vertical range. Most of the values are found by trial-and-error and optimized to capture MLH as good as possible for different weather conditions. An overview of the parameter values is given in table 5.1

| Parameter | value |
|---|---|
| **Gaussian smoothing** | $\sigma = 1.1$ rangegates |
| **Convective delay** | 3 hours |
| **Guiding restrictions:** | |
| **clouds** | $> 5 \times 10^{-3}\ m^{-1}sr^{-1}$ |
| **negative gradient** | $> 5 \times 10^{-4}\ m^{-2}sr^{-1}$ |
| **positive gradient morning** | $< -1 \times 10^{-5}\ m^{-2}sr^{-1}$ |
| **positive gradient day** | $< -2 \times 10^{-4}\ m^{-2}sr^{-1}$ |
| **maximum height night** | 750 $m$ |
| **maximum height day** | 3000 $m$ |
| **minimum height** | 175 $m$ |
| **Graph:** | |
| **window size** | 15 minutes (30 timesteps) |
| **vertical range 1-to-1** | 5 rangegates |
| **vertical range total** | 2 rangegates |

***Table 5.1. Overview of parameters for the Pathfinder algorithm applied to LEOSPHERE ALS450 UV-Lidar.***

In section 5.1 several case studies are shown to discuss the estimates of MLH evolution found by the Pathfinder algorithm. These cases will treat MLH under clear sky conditions, a cloud topped ML and MLH during precipitation. For a quantitative measure of the performance of the Pathfinder method, a comparison is carried out against MLH estimates from other instruments in section 5.2. Here, the results of the STRAT2D method are also included. To test the applicability of the algorithm to different weather conditions a comparison to manual MLH estimates for a full year is discussed in section 5.3. To conclude, two sensitivity tests are carried out in section 5.4 to investigate the robustness of the algorithm and sensitivity to different parameters in the algorithm. In theory, the algorithm is applicable to any lidar or even other instruments, but there are some requirements to take into account. More details on this are discussed in section 5.5.

## 5.1. Case studies

### 5.1.1. Clear sky

The first case study shows 20 May 2010: a clear sky day, with a well-developed ML. The backscatter and gradient data, together with the solution for the MLH from sunrise to sunset are given in figure 5.1. For a detailed description of the different features to be recognized in the backscatter data, see figure 2.4 and the explanation in section 2.1. To point out different features of the algorithm, four regions will be highlighted: the period between sunrise and the onset of the CBL, the morning growth of the ML, the 'stable' period of the ML on the middle of the day and break-down of the ML. These regions are shown in figure 5.2.

*Period from sunset to onset of CBL*

From sunset it takes about 3 hours before the ML extends above the overlap region and to become visible in the lidar observations. Because the complete ML is beneath the lidar detection range, the solution tracks a gradient in the stratification of the residual layer as can be seen in figure 5.2a. However, a positive gradient below this negative gradient around 5-6 UTC indicates mixing does not extend to the height indicated by the algorithm. Around 7 UTC, the ML becomes deep enough to be

visible by the lidar and the solution immediately indicates the correct altitude as MLH. After that it vanishes and reappears about 20 minutes later. The solution again indicates this height as MLH.

*Morning growth of ML*

The greatest challenge to correctly estimate the MLH in the morning growth of the ML, is to separate the gradient associated with the ML from the gradients in the residual layer. When a strong gradient exists close to the gradient of the MLH, a low total path weight can also be found when the algorithm includes these in the estimate. But because the vertical range between timesteps is limited, the algorithm cannot jump to this gradient directly and has to include several points in its path with low gradients. This increases the total path weight, making such transitions a trade-off between the strength of the additional gradient and the difference in height with the MLH gradient. As the ML breaks down the residual layer, these different gradients get close together and the algorithm is more likely to trigger on the residual layer. Figure 5.2b shows that for the most part of the morning transition the correct MLH is indicated. Only around 8:45 UTC the solution indeed triggers on a gradient in the residual layer, when the gradient on the real MLH becomes weaker.

*Mid-day ML*

Although the individual thermals of the CBL are also visible during morning growth, the differences between them are even more pronounced mid-day when the height of the ML is more or less stable. Due to slightly different conditions under which thermals form (e.g. differences in temperature and humidity at the ground), the thermals reach different altitudes. As shown in figure 5.2c, the difference in altitude between subsequent thermal are in the order of 100 to 500 meters, while the average MLH is nearly constant. The vertical limitation of 75m between timesteps is enough to follow the changes in MLH between thermals, like the sudden decrease around 11:15 UTC and the large increase around 12:45 UTC.

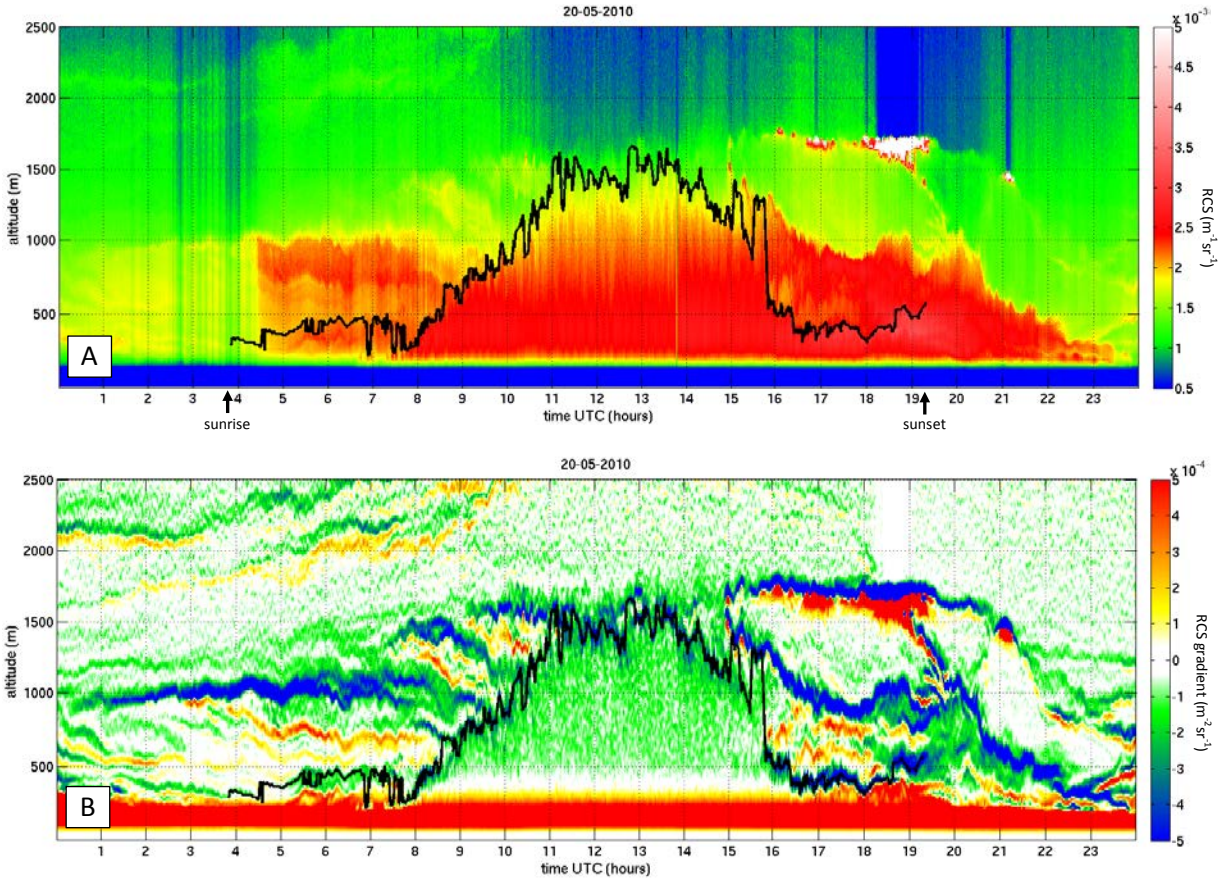


***Figure 5.1. Lidar RCS (above) and gradients (below) together with Pathfinder MLH estimate on 20 May 2010. An almost completely clear-sky day except for the clouds between 16 and 19 UTC.***

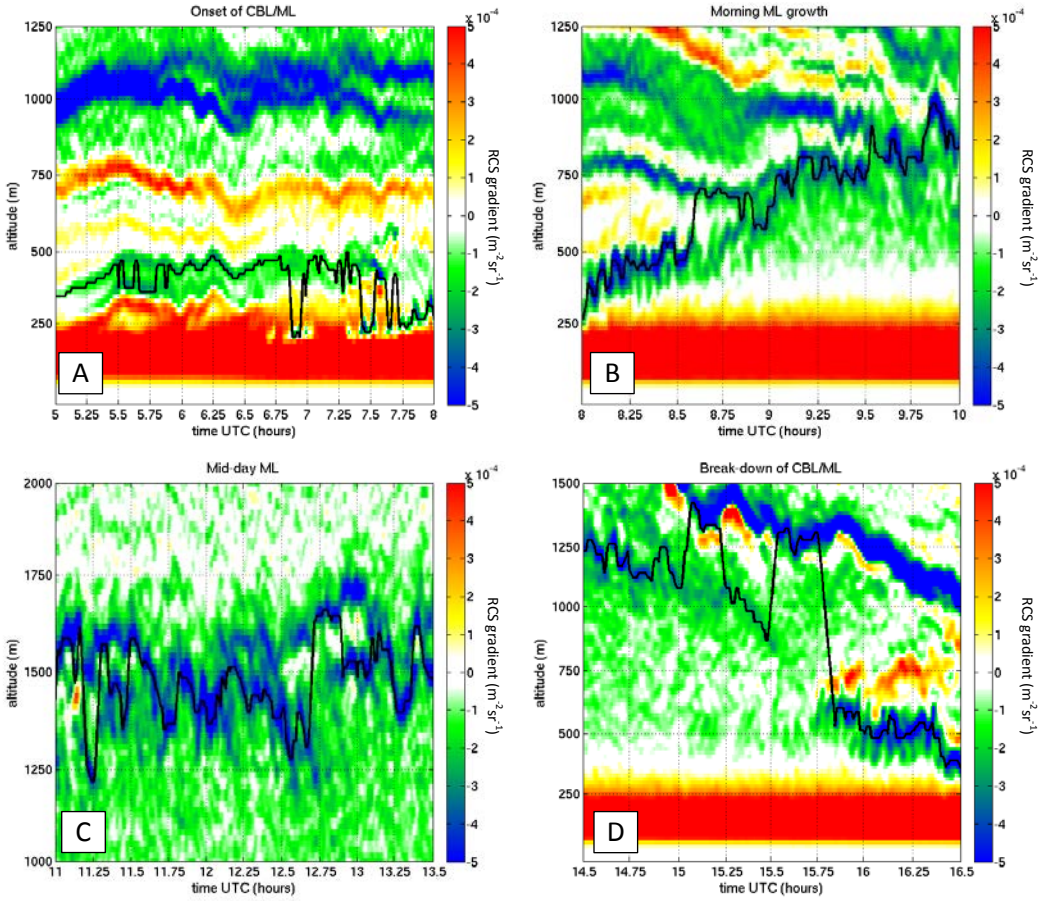


***Figure 5.2. Highlights of the MLH evolution. Gradients in the RCS and Pathfinder MLH estimate during a clear sky day. These include a) the period between sunrise and onset of the ML, b) the morning growth of the ML, c) the mid-day structure of the MLH and d) the break-down of the ML. Time is indicated in decimal hours.***

### *ML break-down*

From 14 UTC onwards, the depth of the ML is no longer stable and starts to decrease in depth. The solution found by the algorithm closely follows this decrease. However, at 15 UTC the gradient at the MLH weakens and becomes nearly indistinguishable from the background (see figure 5.2d). Also, a residual layer is formed at 1400 m, the altitude the convection reached earlier that day. Because the gradient on top of the residual layer is relatively strong, the solution jumps from the MLH to the residual twice, when the gradient on the MLH becomes too weak to be picked up by the guiding restrictions. Eventually, the restrictions force the solution to the right MLH around 16 UTC. The solution calculates the right MLH up to 18:30 when the aerosol concentration near the ground becomes lower than the layers above. As this situation is not accounted for in the algorithm, it keeps tracking the negative gradient leading to a wrong estimate at the end of this day.

Overall, the algorithm almost completely tracks the MLH from the moment the depth of the ML exceeds the overlap region of the lidar near the ground. Most of the gradients in the residual layer are ignored in the morning growth and afternoon break-down of the ML when the vertical distance between gradients on the RL and ML is limited. Large jumps are prevented by exclusion of additional gradients by the guiding restrictions and high weights of measurements between different gradients. But at the same time, the algorithm is able to follow the rapid variations in MLH between the individual thermals.

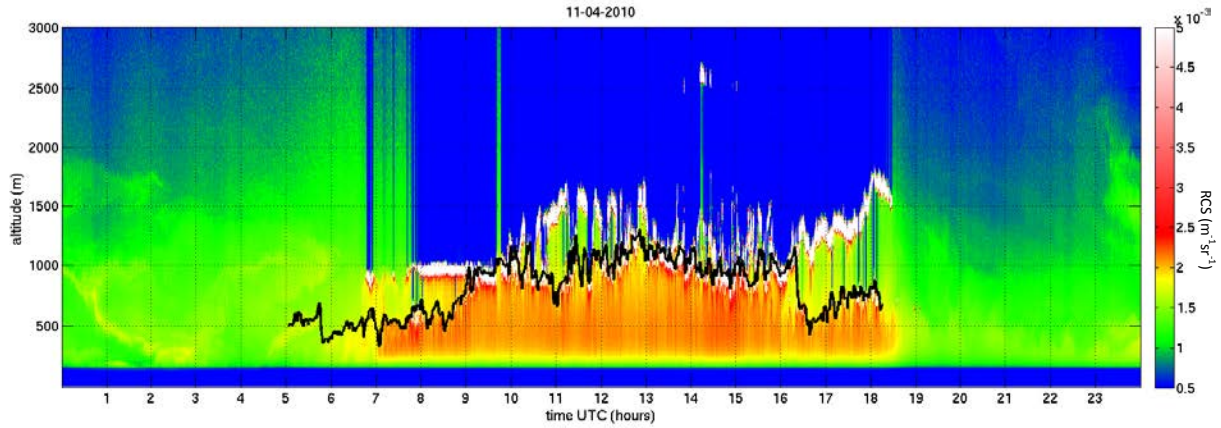


***Figure 5.3. Lidar RCS together with Pathfinder MLH estimate on 11 April 2010. A day with cumulus cloud forming on top of the ML with an additional stratocumulus cloud layer above.***

### 5.1.2. Clouds

Even though a clear-sky day can give a good insight in different features of the ML, complete cloud free days do not occur often in the Netherlands. The presence of clouds influences the evolution of the ML and cause additional gradients which can distract the algorithm from the correct solution. As an example of this, the next case study treats a day with abundant fair-weather cumulus clouds. As can be seen in figure 5.3 two layers of clouds are present, mainly stratocumulus above cumulus clouds forming on top of the ML.

*Multiple cloud layers*

At the beginning and the end of the daylight period the two cloud layers are well separated and the algorithm correctly designates MLH at the lowest cloud layer. Because the cloud deck on top of the ML is broken, the guiding restrictions cannot exclude the stratocumulus clouds for all timesteps. However, the combination of a restricted searching range for the timesteps with clouds present and a limited vertical range is enough to correctly estimate MLH for all timesteps. With the growth of the ML, the distance between the two cloud layers decreases up to a point where the two layers can no longer be distinguished from each other. When the distinction between the cloud layers is unclear, the guiding restrictions cannot exclude the second layer and the solution tracks the top of the highest clouds as MLH, leading to short peaks in the MLH, e.g. around 10 and 10:45 UTC (figure 5.4a).

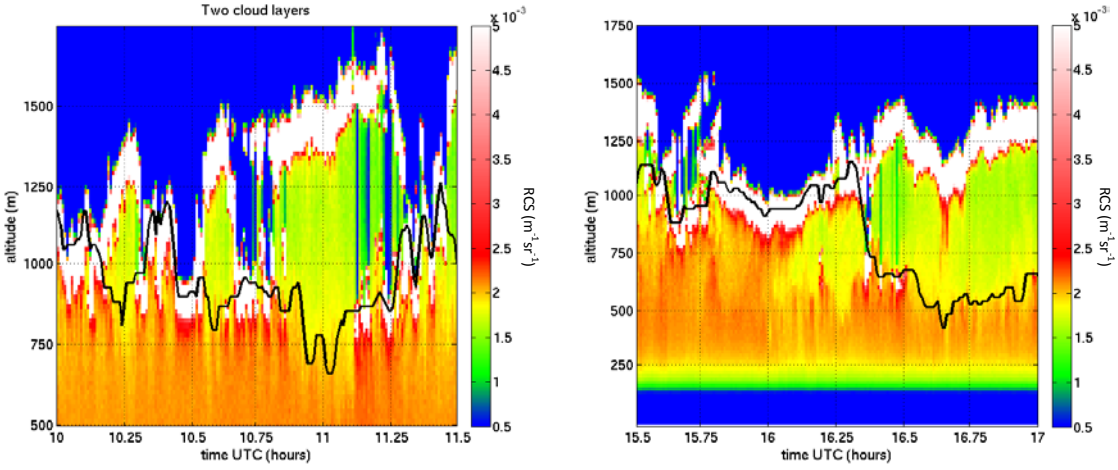


***Figure 5.4. Highlights of the MLH estimate found by the Pathfinder algorithm. Shown are a) difficulties in distinguishing ML and non-ML clouds and b) commitment to a cloud layer that dethatches from the ML.***

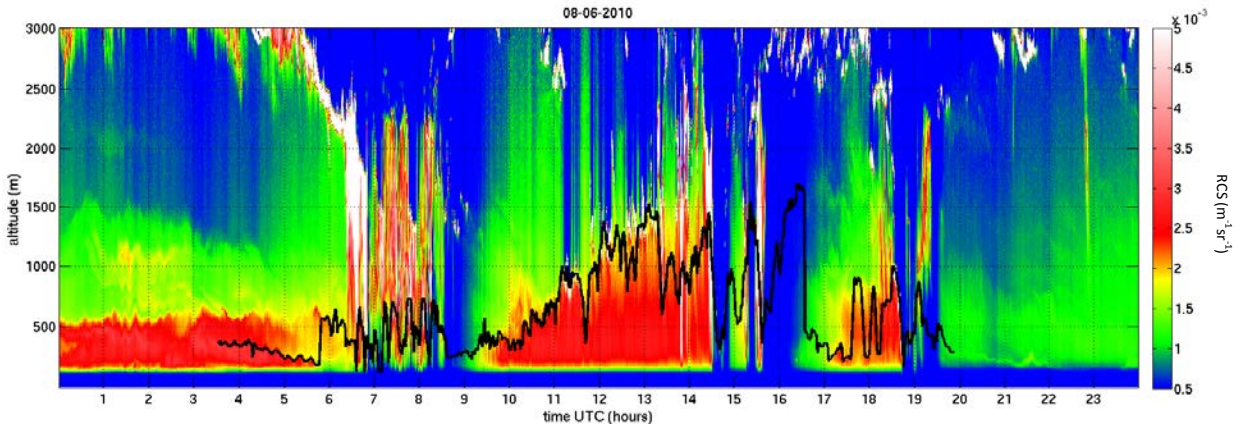


***Figure 5.5. Lidar RCS together with Pathfinder MLH estimate on 8 June 2010. A day with several types of cloud and precipitation affecting the lidar measurements.***

*Commitment to a cloud layer*

An example of the solution following the wrong cloud layer can be seen in figure 5.4b between 15:45 and 16:15 UTC. The ML decreases in depth, but a cloud layer remains at the same altitude. In this case, a jump from this cloud layer, down to the correct MLH is needed. Instead, the solution keeps tracking the cloud layer until clouds form on top of the ML. These are detected by the guiding restrictions and only after that, the algorithm returns to the real MLH. Because the algorithm is designed to track gradients close to adjacent gradients, the shortest path algorithm will not divert the MLH estimate from a cloud layer. For this, the algorithm needs either clouds or a strong gradient to trigger the guiding restrictions.

### 5.1.3. Rain

The last cases consider the ML during precipitation. This poses an extra difficulty to the algorithm because the water on the instrument attenuates a large part of the signal. Next to that, high lidar backscatter on raindrops obscures the cloud base and aerosol structures in the rain. Also, the MLH changes rapidly during the rain. As air descends in the downpour there is a decoupling between the surface and the local air above. Rain also cools down the surface and changes the energy balance so that mixing from the surface reaches to lower altitudes.

*Effect of rain on the instrument*

An example of a day with precipitation is 8 June 2010 and shown in figure 5.5. After (heavy) precipitation, the observations of the lidar are affected by water on top of the instrument. Only the backscatter on clouds is high enough to be distinguished from the background signal and noise. An estimate based on these lidar measurements is unreliable if not impossible. During the rain between 6:30 and 8:30 the MLH estimate fluctuates between 150 and 750 m, the complete range allowed by the restrictions. Also, after the short rainshowers around 14:30 and 15:30 UTC, the quality of the lidar measurements are too low to calculate a reliable MLH estimate.

*Meteorological effects*

Another day with frequent precipitation is 20 June 2010 (see figure 5.6). But this precipitation did not affect the quality of the measurements because mostly it did not reach the surface but evaporated before reaching the ground. The intensity of the lidar backscatter is only diminished for a short period between 12:00 to 1:30 and 3:30 to 4:30 UTC, the only periods where the precipitation actually reached the ground. A total of only 0.2 mm rain was observed in Cabauw the complete day. With a lot of precipitation not reaching the ground, this day gives more insight in the effects of precipitation on the ML and the MLH solution of the Pathfinder algorithm in these situations.

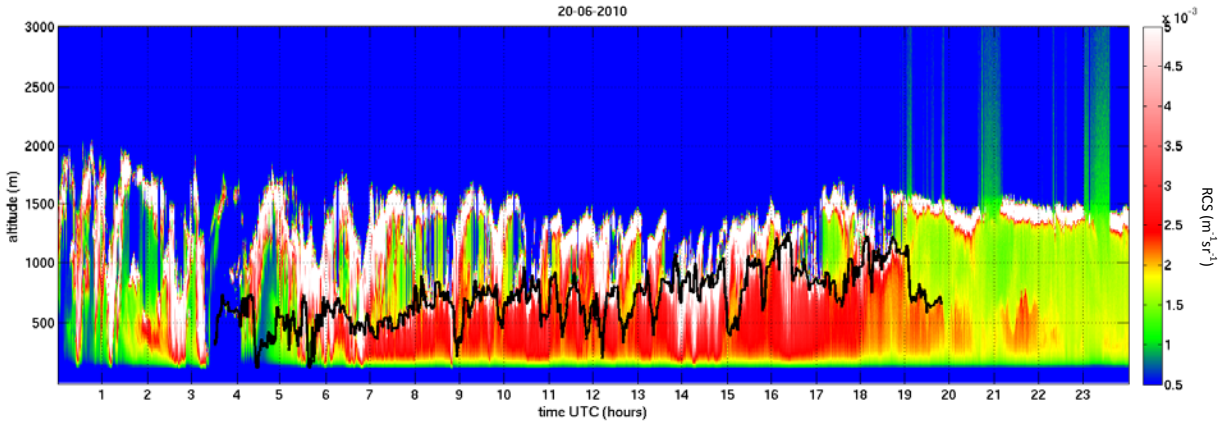


***Figure 5.6. Lidar RCS together with Pathfinder MLH estimate on 20 June 2010. A day with a completely overcast sky and precipitation falling from the cloud but evaporating before reaching the surface.***

Similar to the case in section 5.1.2, two layers of clouds are present in this case. For the periods without precipitation, the algorithm correctly picks the top of the lowest cloud layer as MLH, e.g. between 7 and 9 UTC. The precipitation events occurring during the day can be grouped into two categories: precipitation evaporating in the overlap region of the lidar or precipitation evaporating well above it. The period between 14 and 15 UTC, shown in figure 5.7a, is an example of precipitation reaching the overlap region. Because the raindroplets evaporate during their fall, the highest droplet concentration is found near cloud base and decreases closer to the surface. As a result, lidar backscatter increases with altitude and no negative gradient is found in the downdraft. Without a negative gradient under the cloud, the algorithm can only find a path on top of the cloud (or the visible part of cloud when the signal is completely attenuated). This altitude is than indicated as MLH, although the height of the ML does not reach to the top of the clouds. This can be seen after 15 UTC when the precipitation stops. Without the rain droplets dominating the signal, a ML becomes visible with a height of almost 500 m, a lot lower than the clouds.

An example of a precipitation evaporating well above the surface can be seen in figure 5.7b. From this example it is clear that the ML is lowered by precipitation. Around 11:15 UTC, precipitation appears and with it, the high backscatter of the ML decreases in altitude. When the precipitation clears, air is no longer brought downward in the downdraft, the ML increases again in altitude. The gradient on top of this layer is picked up well by the Pathfinder algorithm. Similar events can be observed between 11:45-12 UTC and 12:30-13 UTC.

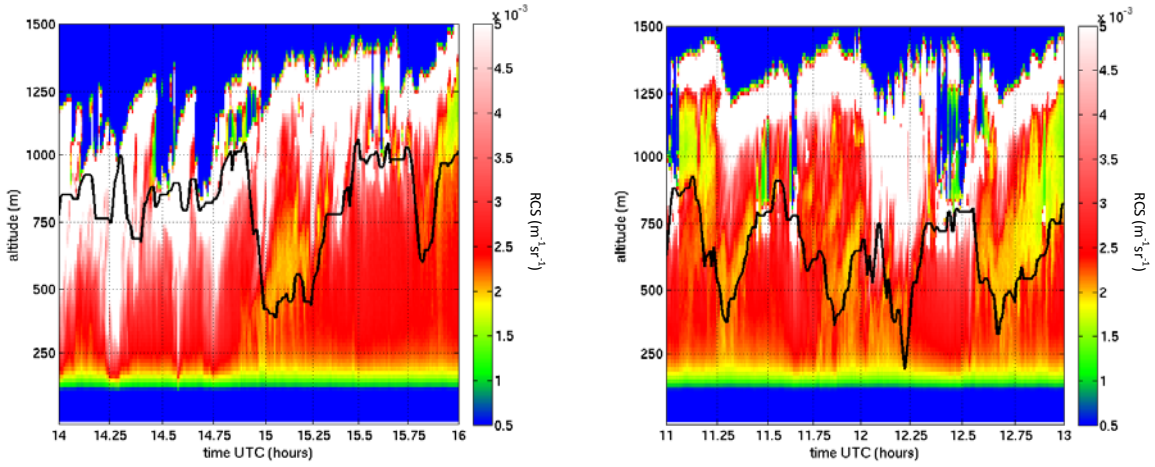


***Figure 5.7. Highlights of the MLH estimate found by the Pathfinder algorithm on 20 June 2010. Shown are a) precipitation events reaching the overlap region and b) precipitation evaporating well above this region.***

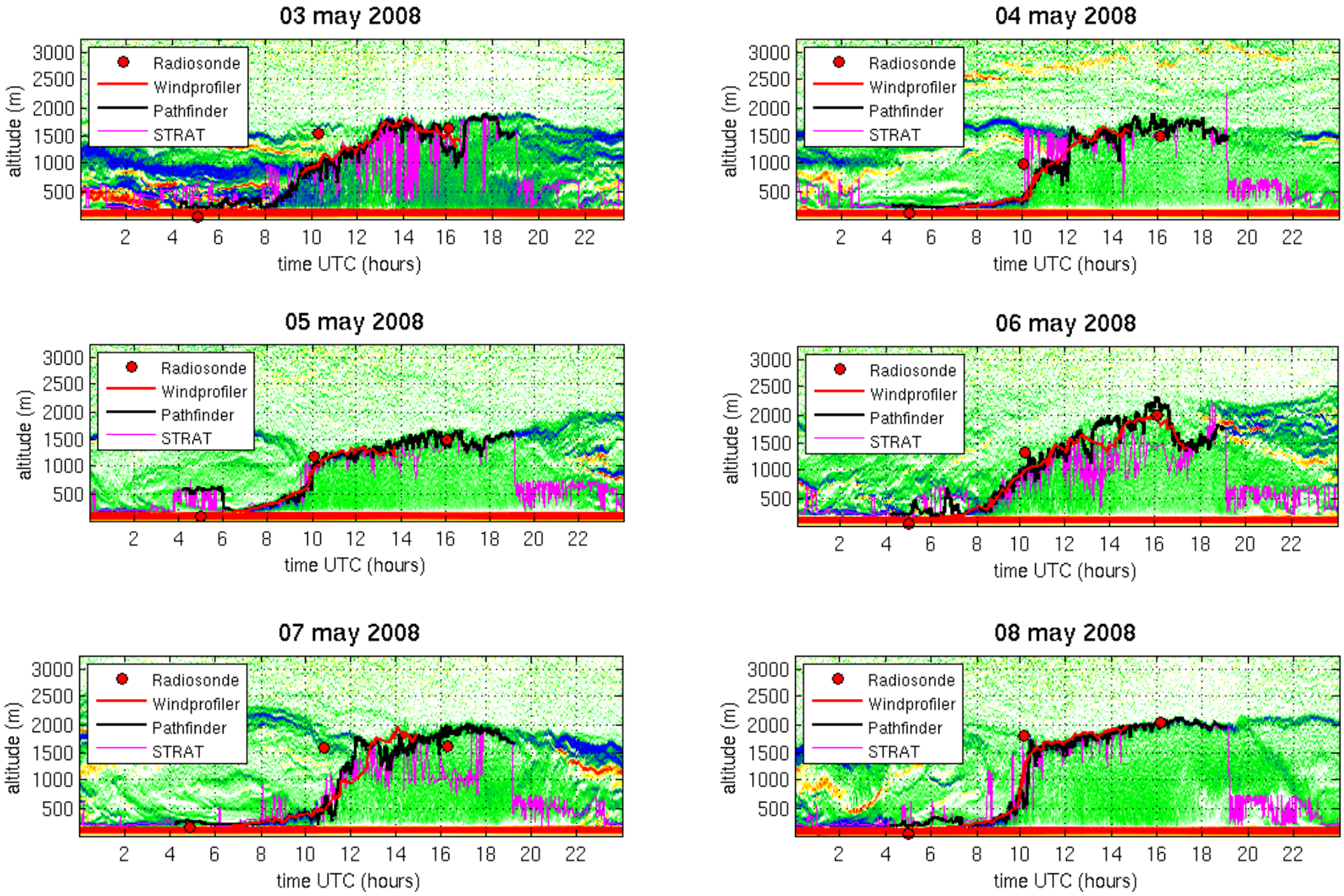




***Figure 5.8. Overview of the 12-day period during the IMPACT campaign at Cabauw. Shown are the lidar RCS together with MLH estimates from radiosonde (red dots), windprofiler (red line), Pathfinder method (black line) and STRAT2D method (magenta line)***

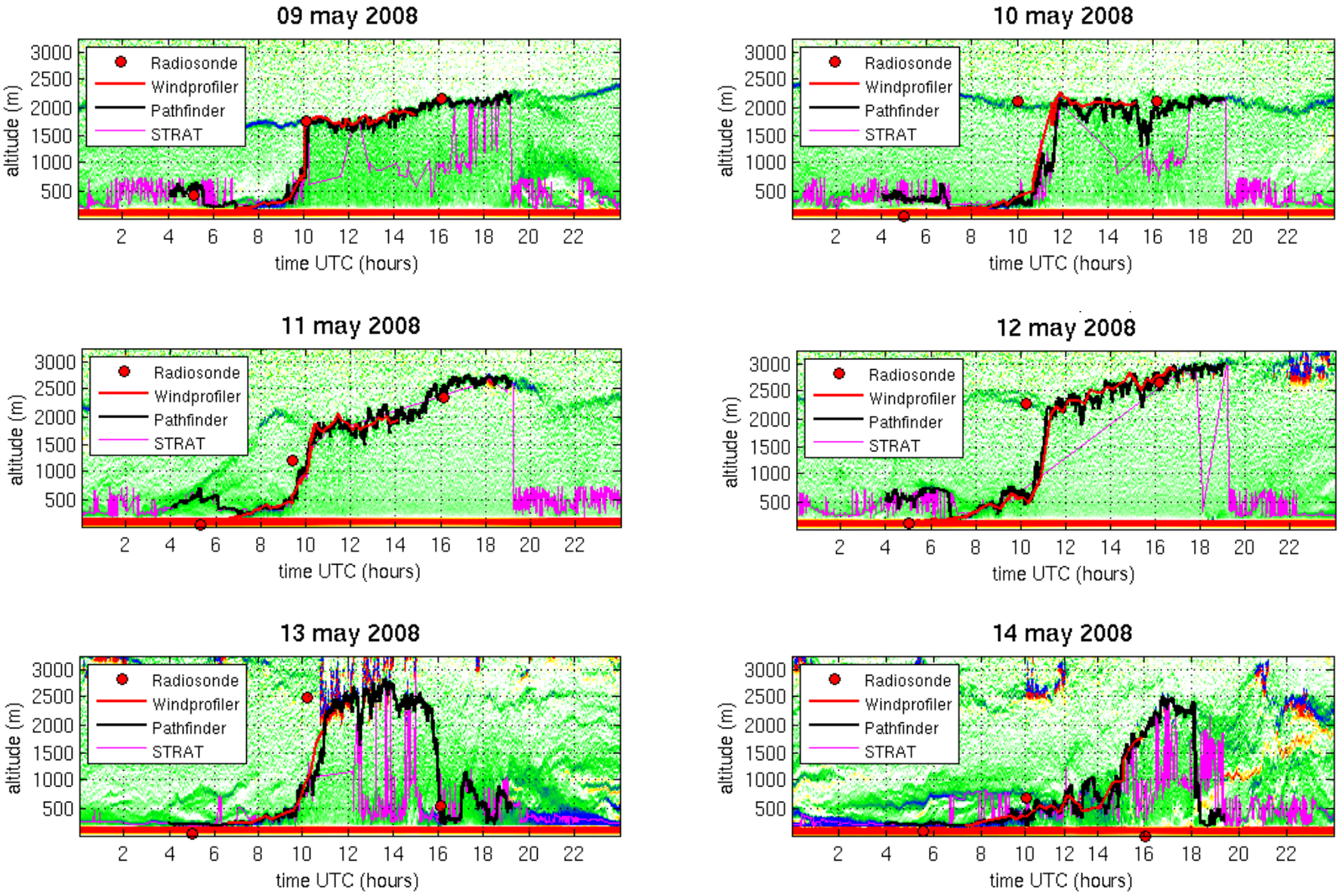




*Figure 5.8. (continued) Overview of the 12-day period during the IMPACT campaign at Cabauw. Shown are the lidar RCS together with MLH estimates from radiosonde (red dots), windprofiler (red line), Pathfinder method (black line) and STRAT2D method (magenta line)*

## 5.2. Performance compared to other instruments

To further test the Pathfinder method and to get a quantitative measurement of its performance, a comparison is made with MLH estimates from radiosonde and windprofiler. Observations for this are taken during a 12 day-period in May 2008, part of the EUCAARI IMPACT campaign at Cabauw. The radiosonde observations are taken around 5, 10 and 16 UTC each day. The Richardson bulk method (see section 2.2) was used for estimates for these soundings. The windprofiler operated continuously, but MLH estimates are only given for the above-mentioned 12-day period and limit this comparison. The ALS450 also operated continuously and both our new Pathfinder method and the STRAT2D method are used to derive MLH. A complete overview of the different timeseries is shown in figure 5.8.

*Comparison with windprofiler*

First, we will compare the new Pathfinder method and the windprofiler. The MLH estimates from both instruments have an excellent agreement, being within a vertical range of 100m of each other for almost the complete period. Exceptions are found for short periods around 14 UTC on 6 May, 12 UTC on 7 May, 11 UTC on 10 May and 14 UTC on 14 May. Next to that, the Pathfinder algorithm is unable to track the shallow ML in the mornings of 5, 9 10, 11 and 12 May when the ML is under the detection range of the lidar. On 6, 11 and 12 May, the windprofiler picks up this shallow ML a few hours earlier than the Pathfinder method. Overall there is a very good agreement ($R^2 = 0.96$) between the overlapping estimates of the two methods.

*Comparison with radiosonde*

Between the Pathfinder estimates and radiosonde estimates the agreement depends on the time of the day. It is good ($R^2 = 0.90$) for the 16 UTC soundings, but questionable for the 5 UTC and 10 UTC soundings. At the 5 UTC soundings, the ML is mostly too shallow to be picked up by the lidar. As a result, the correlation between the instruments is low: $R^2 = 0.21$. Comparing the 10 UTC soundings with the lidar observations, it becomes clear that the Richardson bulk method calculates the top of the residual layer as MLH on e.g. 10 and 12 May. Investigation of these soundings (figure 5.9) shows that theoretical air parcels rising from the ground indeed have positive buoyancy almost up to 1400m. The Richardson bulk method estimates MLH somewhat above this altitude due to effects of wind shear. Also shown in the temperature profile is a nearly well-mixed layer up about 900 m. This altitude is also registered as MLH by the Pathfinder method. Based on this, it can be concluded the Pathfinder method calculates the correct MLH in this case and the radiosonde method does not. This is probably caused by the fact the radiosonde method does not take into account entrainment of colder ML air into the rising parcel. Because of the lower temperature, the parcel loses its buoyancy at a lower altitude and does not ascend up to the altitude predicted by the radiosonde methods. Ignoring entrainment for deep convection, where the largest part of the ascent takes place in non-turbulent FA air, might be appropriate, but because of the turbulent nature of the ML, entrainment takes place at a much higher rate and cannot be neglected.

*Comparison with STRAT2D method*

Finally, we will look at the results (see figure 5.8) of the STRAT2D for this period. For a large part of the timesteps, the MLH found by the STRAT2D method corresponds to the results of the windprofiler (and Pathfinder method). For 5 and 8 May the paths correspond almost perfectly. But because the STRAT2D method treats every timestep independently, large differences in MLH are found for subsequent timesteps when the largest gradient is found on irregularities within the ML. This leads to an unrealistic, erratic evolution of the MLH during the day. Additionally, the STRAT2D method often misses estimates due to the criterion of the ratio between the backscatter above and below the MLH

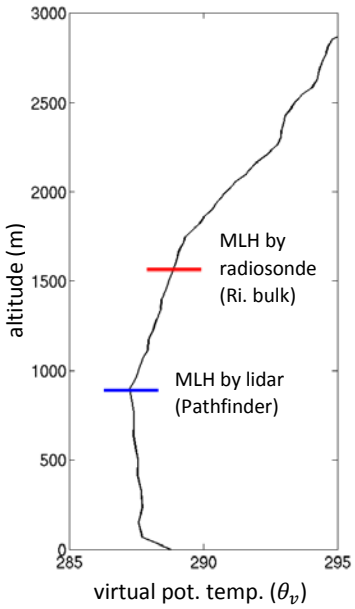


***Figure 5.9. Vertical profile of virtual potential temperature $\theta_v$ on 3 May 2008, 10 UTC, based on radiosonde measurements. Shown in red is the MLH estimate by the Richardson bulk method. Shown in blue is the MLH estimate by the Pathfinder method.***

(see the description of the method in section 3.4). In the considered period, the air in the ML was relatively clean and backscatter in the ML not high enough compared to the FA to fulfill this criterion. Thus, although the situation is straightforward, without much interference by clouds, structures in the RL or rain, the STRAT2D fails to give a good estimate for the MLH on these days.

## 5.3. Comparison with manual MLH estimates

To test the applicability of the algorithm for different weather situations, it has to be applied to a longer time series and compared to another method, preferably based on a different instrument for an independent evaluation. As continuous measurements are needed for this comparison the best option were the 12UTC radiosonde observations of De Bilt (30 km from Cabauw), despite the distance between the observations and the difficulties in the morning transition shown in previous section. Other instruments were not available for comparison because these were not continuously operated or not equipped with a method to derive MLH.

Before using the radiosonde observations, they were checked against manually derived MLH estimates based on the lidar measurements at Cabauw (this procedure will be discussed below). Comparison indicated that the radiosonde measurements at De Bilt were not representative for the MLH at Cabauw. The correlation coefficient between the radiosonde estimate and the real MLH for the complete year 2010 was $R^2 = 0.64$, with an average difference of more than 200 meters.

To still be able to get a quantitative measure for the performance of the Pathfinder algorithm manual estimates based on the lidar estimates were used. To imitate the frequency of radiosonde observations an estimate was made for the MLH at 12 UTC for each available day in 2010. Lidar RCS and gradient fields were visually inspected to get an indication of the weather conditions and the evolution of the boundary layer during that day. With this information, a closer view of the measurements around 12 UTC were used to pinpoint the exact location of the decrease in backscatter associated with the MLH. Of the 336 days with available measurements, manual MLH estimates could only be made for 252 days. On the other days, the lidar measurements had insufficient quality to derive MLH, caused by mechanical problems or weather conditions like rain or fog.

The Pathfinder method was also applied to all days in 2010 with available lidar measurements. For each of those days, MLH is calculated from sunrise to sunset. To be able to compare the outcomes,

an average MLH was calculated of the Pathfinder estimates between 11:55 and 12:05 UTC. These averages were then compared to the manual MLH estimates and correlated well with the manually derived MLH ( $R^2 = 0.90$). The average offset of the Pathfinder estimate was 76 m (see the left panel of figure 5.10). Because the quality flag ratio gives an indication of the reliability of the estimates, it can be useful to make a selection of the MLH estimates based on this ratio. Excluding the estimates with a backscatter ratio above 0.9, leads to a comparison of 196 days yielding a correlation coefficient of $R^2 = 0.96$ and an average offset of 52 m. Although the reliability of the estimates increases with the selection, it also excludes correct estimates.

To investigate whether the Pathfinder algorithm performs better than other lidar-based methods, the estimates of STRAT2D are compared to the manual estimates in a similar way. Because the STRAT2D algorithm only gives a value for MLH if the backscatter ratio is lower than 0.9, no additional selection can be made based on this ratio. On the other hand, some days are already missing an estimate on 12 UTC. In total 235 days are compared, leading to a correlation of $R^2 = 0.74$ and an average difference of 127 m with the manual estimate.

As shown in the right panel of figure 5.10, the STRAT2D method has considerably more scatter than the Pathfinder method. For most of these bad estimates STRAT2D calculates a higher MLH than the manual procedure. In these cases STRAT2D picks the gradient of top of the residual layer as the MLH. Even with the quality criterion based on the backscatter ratio, the STRAT2D method is less capable of rejecting these estimates.

This full-year comparison of MLH estimates also indicates that MLH exhibits an annual cycle. The color coding in figure 5.10 shows that the lowest MLH values are found in the winter months and the highest values in spring and summer. More information on this annual cycle, but also the daily cycle of MLH is discussed in section 5.6.

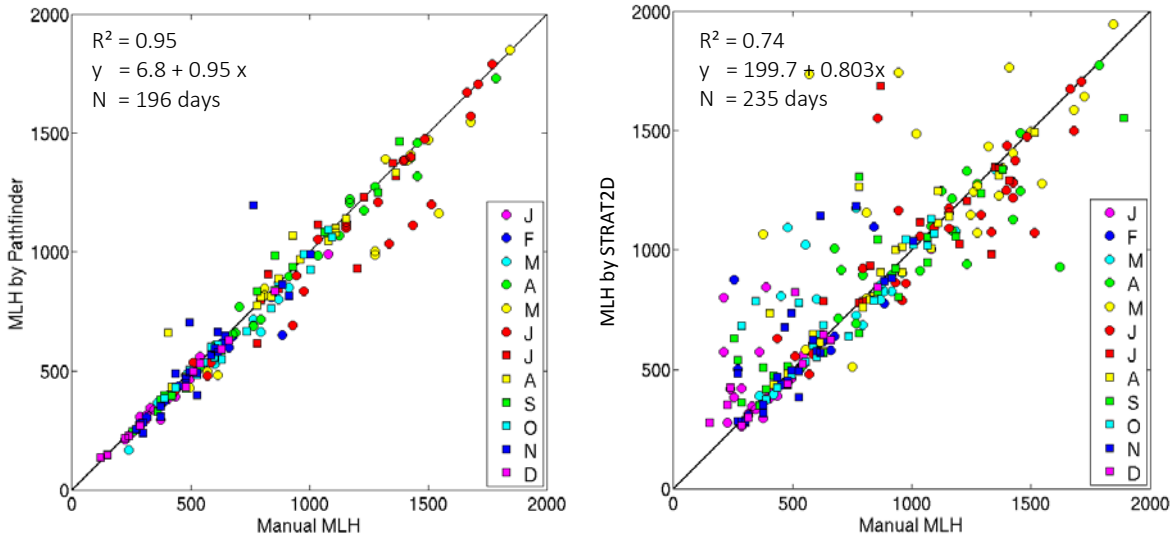


***Figure 5.10. Comparison MLH estimate of Pathfinder method (left) or STRAT2D method (right) and manual MLH estimate at 12 UTC for the year 2010. Only days with a sufficient backscatter ratio*** $(B < 0.9)$ ***are shown. The color coding indicates the month in which a MLH estimate is taken.***

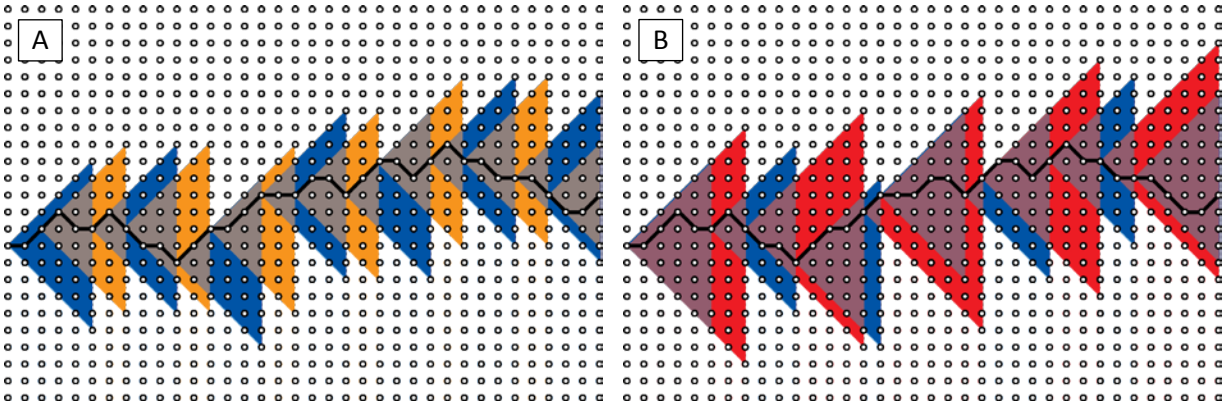


***Figure 5.11. Simplified representation of the differences in included measurement points for the search for MLH using a) different starting points or b) different window sizes. The blue triangular areas are the same in both examples.***

## 5.4. Sensitivity studies

One of the strengths of the Pathfinder method to find the correct MLH is limiting the search to measurements around previous MLH estimates. With this, the part of the measurements included in the search depends on this (pre-described) vertical range. This makes this strength also a weakness of the algorithm. A path can lead the solution away from the real MLH, e.g. on a residual layer or noise induced gradients. If this path is too far away from the real MLH, it does not include the 'correct' solution might diverge. This raises a question on how sensitive the method is for changes in the allowed range.

Two parameters are changed to test this sensitivity: the amount of timestep considered simultaneously or the selection of the first timestep. Within a time window, the search range expands with 75m each step forward in time and the range of measurements considered in the search for MLH increases accordingly. When the path in one window is calculated, the search range resets and increases again from the first step in the new window. When the position of the first time step is changed, the size of the searching range remains the same, but shifts along the time axis. When a day is divided into larger windows, the searching range expanding further from a starting point and a larger part of the measurements is included. A graphical representation of these changes is shown in figure 5.11.

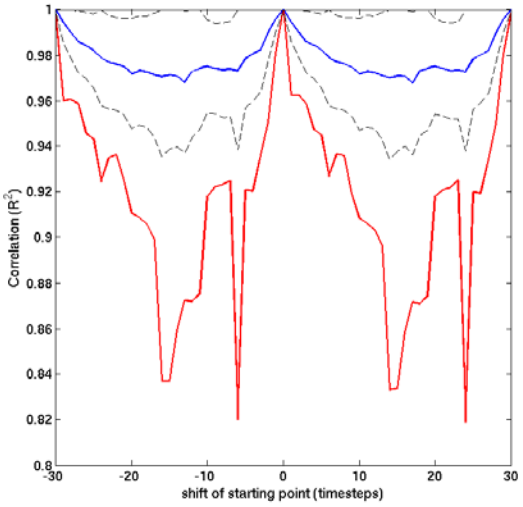


***Figure 5.12. Correlations of additional runs with shifted starting points with the default run. Shown are the average correlations (blue) of all days in May 2010 for a certain shift in starting point. Also shown is the band of $\pm$ 1$\sigma$ (dashed) and lowest correlations (red) found on individual days.***

### 5.4.1. Different starting points

With the default time window size of 15 minutes, 30 timesteps are considered simultaneously for the measurements of the ALS450 UV-lidar. To test the sensitivity to a shift of the starting point the algorithm was applied 61 times to the observations of one day. Next to the default calculation starting at the first timestep after sunrise, 30 additional calculations were performed with a starting point shifted backwards 1 to 30 timesteps and another 30 calculations with a starting point shifted forward 1 to 30 timesteps.

This analysis is applied to the UV-lidar observations of May 2010. This month consisted of both sunny and cloudy days. The month was relatively dry, but precipitation occurred on 6 days of the month. Figure 5.12 shows the correlations of the additional calculations with the default calculation. This is the correlation between the MLH estimates of a full day, averaged over all days in May 2010. Next to the average, the lowest correlation is shown as well. The average correlation is very high and does not drop below $R^2 = 0.96$. Another measure of the sensitivity of the algorithm is the ratio of exact same MLH estimates as the default calculation. Again, this was the lowest for a shift of 17 timesteps forward, but still 93% of the MLH estimates on a day corresponded exactly with the default calculation.

Looking at the average correlations, the lowest correlations are found for shifts around 15 timesteps, either forward or backward. This is a result of the amount of overlap between the calculations, which is minimal for shifts of half the window size. Because the shape of the searching range repeats itself, a shift of more than half the window size is identical to a shift from the previous of next time window, provided that the solution is similar. The additional variation in the correlation depends on the exact structure of aerosol and cloud layers.

The lowest overall correlation was $R^2 = 0.82$ for the calculation on 30 May with a backward shift of 6 timesteps. Solutions of both the shifted and default starting point derived the same MLH except for the period between 15 and 18 UTC (see figure 5.13). During this period, the lidar signal was weakened due to precipitation. Actually, during this period both calculations did not derive the correct MLH as can be seen from the backscatter around 16:45 UTC, where the top of the ML appears around 400 m. The large difference between 16:15 and 17 UTC originates at 16 UTC where the solutions start to diverge. Due to this, the additional calculation did not pick up the gradient under the rain shower at 16:15 UTC. Instead it tracked a path of gradients to the top of the clouds at 2500 meters. The original calculation did not, because this path was outside the searching range. At 17 UTC, when the signal returned to its full strength, the guiding restrictions forced both solutions

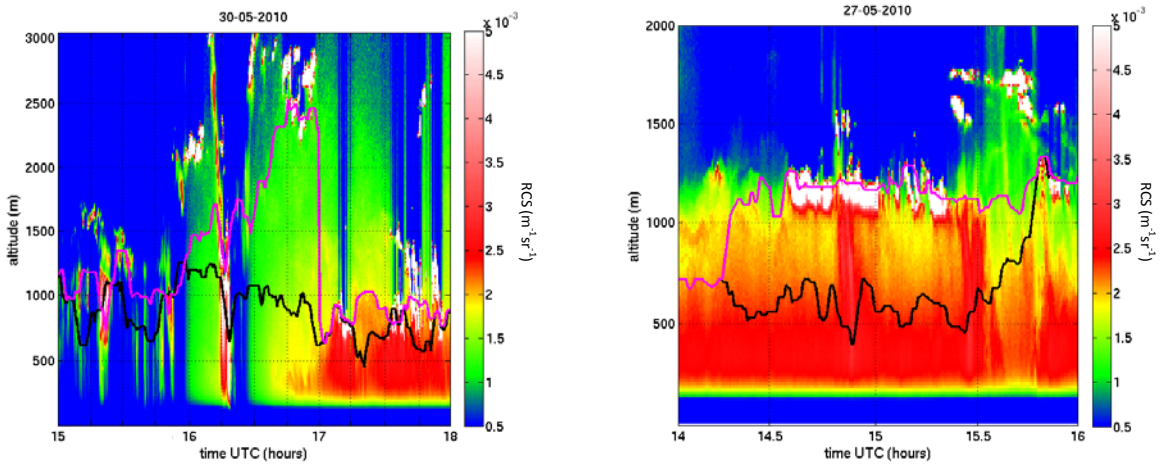


***Figure 5.13. Highlights of changes in the MLH estimate found by the Pathfinder algorithm for changes in a) starting point and b) time window size. Default MLH estimates are shown in black, additional estimates are shown in magenta.***

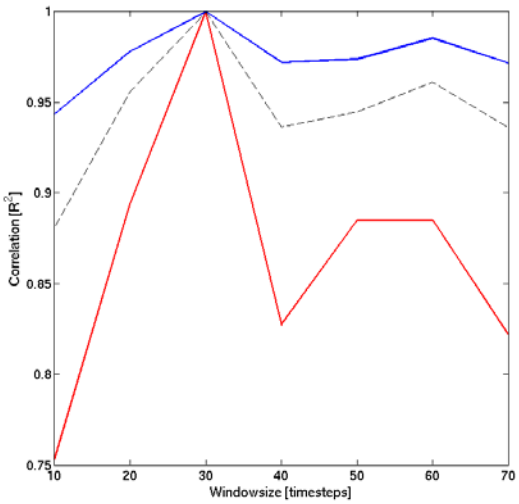


***Figure 5.14. Correlations of daily MLH estimates between the default window size of 30 timesteps and additional runs with different time window sizes. Shown are the average correlations (blue) with a band of $\pm$ 1$\sigma$ (dashed) and minimum correlations (red) of all days in May 2010 for different window sizes.***

back to the MLH. After tracking the same path for several timesteps, the two calculations gave different results again because of multiple layers of gradients. The default calculation tracked the MLH, whereas the additional calculation tracked the top of a residual layer with high aerosol concentrations. Even though the method seems to be unstable in the examples, these periods of disagreement are usually short and estimated MLH is exactly the same for at least 76% of the timesteps on a full day. In all, changing the starting point does effect the solution but only to a small extent. The solution can diverge for short periods due inclusion of other gradients into the searching range of the shortest path algorithm. However, the guiding restrictions force the solution back to the correct MLH and the general evolution of MLH is similar for all starting points.

### 5.4.2. Different window sizes

A second series of tests investigates the sensitivity of the solution for changes in size of the time window. Next to the default time window of 30 timesteps, additional calculations used window sizes increasing from 10 to 70 timesteps, with increments of 10 timesteps. Increasing the time window above 70 was impossible because of computing limitations. Similar to the analysis of different starting points, the observations of May 2010 were used.

An overview of the results is shown in figure 5.14. Average (minimum) correlation coefficients are around 0.975 (0.85) except for the window size of 10. The lowest correlations for the larger timesteps all occurred on the same day: 27 May 2010. Besides some small differences, this is due to the period between 14 and 16 UTC. Two different tracks were found by the calculations as shown in figure 5.14b.

The cause of this division of the solutions in two groups is the size of the searching range. All solutions track the correct MLH before 14:15 UTC. Starting from this altitude, a larger time window includes the residual layer and clouds are included in more timesteps. For each time window, the algorithm has to include several high weights to allow a jump to the residual layer. For the smaller time windows however, there are not enough timesteps left after the jump to counteract the high weights from the jump. In case of the large time windows, there are more timesteps left after the jump and the track to the residual layer gets the lowest overall weight. In this situation, the calculations up to a window size of 30 calculated the lower track, but the calculations with larger window sizes tracked MLH along the cloud tops.

All measurements that can be reached by a change of 2,5ms$^{-1}$ from the starting point of a timewindow are considered for MLH. This ensures the algorithm captures changes between thermals. But to limit the algorithm to track a gradual evolution of MLH over longer timescales, the

*Figure 5.15. Pictures of the Vaisala-Impulsphysik LD-40 ceilometer at Cabauw (left) and the HALO Photonics Doppler lidar at Chilbolton (right). The ALS450 at Palaiseau is similar to the one located at Cabauw, shown in figure 2.1*

last point within a timewindow is limited to a change of $1ms^{-1}$. For the smaller time windows, the limit of $1ms^{-1}$ causes a searching range too small to capture changes in MLH due to individual thermals. As a result many small differences occur between these and the default calculations and the correlation between them decreases. Several runs with a window size of 5 timesteps confirmed this behavior with average correlation coefficient around 0.9 and a minimum below 0.7. Similar to changes in the starting point, altering the time window can cause different solutions. The guiding restrictions ensure these deviations only occur over short periods and force the solution back to the same MLH.

## 5.5. Application to other lidars

Previous sections of this chapter showed the results of the Pathfinder method on the LEOSPHERE ALS450 UV-lidar at Cabauw. However, the method should be applicable to any lidar or other instrument. As long as the measurement values at MLH are sufficiently different from measurements elsewhere, the Pathfinder method should be able to determine the evolution of the MLH.

During this research, the Pathfinder method was applied to three other lidars: a Vaisala-Impulsphysik LD-40 ceilometer, a HALO Photonics Doppler lidar and another LEOSPHERE ALS450 lidar (see figure 5.15). Initially, these measurements were included to perform comparisons of the Pathfinder method. However, comparisons were not possible because these other lidar observations were not suitable for MLH detection by the Pathfinder method (LD-40 and ALS450 at Palaiseau) or requested MLH estimates not available in time (Doppler lidar). Nevertheless, the application to these other lidars still gives insight in the applicability of the Pathfinder algorithm and the requirements to lidar measurements. An overview of the lidars is given in table 5.2.

| Parameter/specification | ALS450 | LD-40 | HALO Doppler |
|---|---|---|---|
| **Transmitted wavelength** | 355 nm | 855 nm | 1550 nm |
| **Pulse repetition frequency** | 20 Hz | 6494 Hz | 15 kHz |
| **Pulse energy** | 12 mJ | 1 µJ | 10 µJ |
| **Pulse duration** | 6 ns | 75 ns | 200 ns |
| **Telescope diameter** | 20 cm | 14 cm | 6 cm |
| **Time resolution** | 30 s | 15 s | 30 s |
| **Height resolution** | 15 m | 7,5 m | 36 m |
| **Location** | Palaiseau, France | De Bilt / Cabauw, The Netherlands | Chilbolton, United Kingdom |

*Table 5.2. Short overview of lidar specifications.*

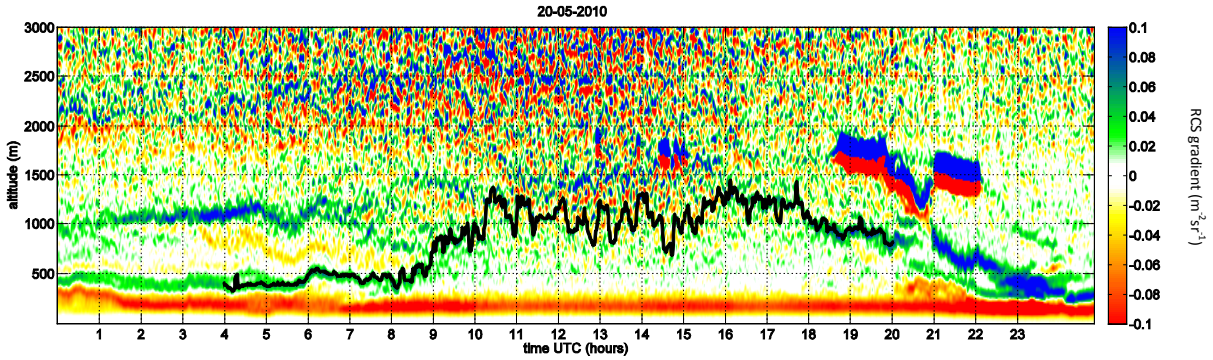


***Figure 5.16. Gradients in LD-40 ceilometer measurements together with Pathfinder MLH estimate at Cabauw on 20 May 2010. Due to the low laser pulse power, noise-induced gradients prevent detection of MLH above 1000 m.***

### 5.5.1. LD40 ceilometer

KNMI operates a network of Vaisala-Impulsphysik LD40 ceilometers at 25 locations in the Netherlands. This network is mainly used for detection of cloud base height for aviation and meteorology. Although not designed for this specifically, these ceilometers can also be used for MLH detection (Haij et al., 2007). One of these LD-40 ceilometers is located at De Bilt and collocates with the radiosonde measurements launched there. As such, these ceilometer observations can be used to further evaluate MLH estimates by radiosonde methods without the distance between the observations. Another LD-40 is operated at Cabauw and gives an opportunity test the performance of the Pathfinder algorithm on LD-40 observations by a comparison to the manual estimates.

The LD-40 operates with a near-infrared wavelength of 855 nm. It has a temporal resolution of 15 seconds and a vertical resolution of 7.5 meters and a measurement range of 25 to 13400 meter. However, the relatively low laser pulse power (1 µJ in 75 ns) limits the range with a sufficient signal-to-noise ratio (SNR) to about 1000 to 1500m, depending on the aerosol concentration in the ML. Especially during spring and summer, this is too low to capture the complete ML.

An example of LD-40 observations and the MLH estimate found by the Pathfinder algorithm can be seen in figure 5.16. It shows measurements of the same day used as the clear sky case in section 5.1.1. Evident from this example is the low SNR above 1500 m. As sunlight is the main sources for this noise, the altitude of a useful signal is even lower at the middle of the day. Because of the strong gradients induced by this noise, the Pathfinder algorithm is not able to track the correct MLH.

Even though the ceilometer network could have provided an excellent opportunity for MLH measurements, the limited altitude SNR makes it difficult to use the Pathfinder algorithm on the LD-40 observations to give a reliable estimate of MLH.

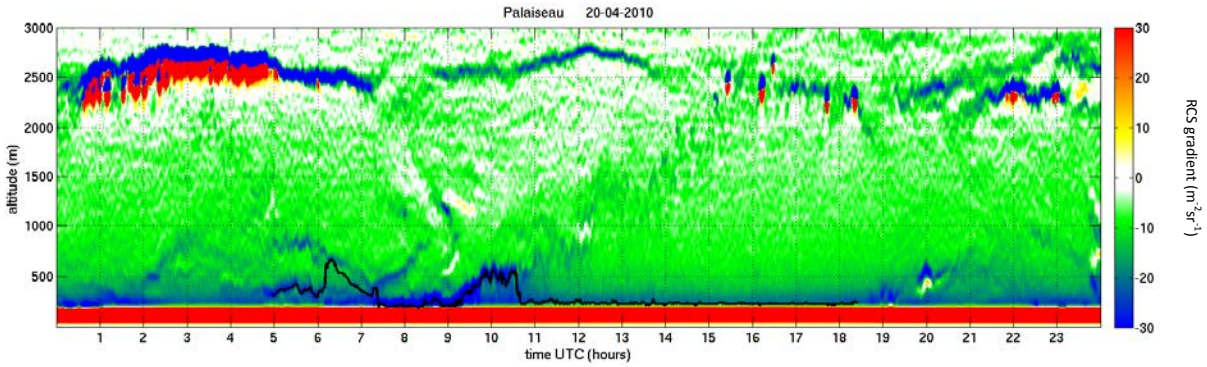


***Figure 5.17. Gradients in ALS450 UV-lidar measurements together with Pathfinder MLH estimate at Palaiseau on 20 April 2010. Due to the strong attenuation of the signal at lower altitudes, the Pathfinder method is diverted from tracking gradients associated with MLH. Compare to the ALS450 measurements at Cabauw in figure 4.2.***

### 5.5.2. ALS450 UV-lidar at Palaiseau, Paris

In another attempt to test the performance of the Pathfinder method, we applied the method to the observations of a LEOSPHERE ALS 450 UV-lidar located at Palaiseau (about 15 km from the center of Paris). The reason for this is that for this location MLH estimates from a new STRAT+ method (Pal et al., 2013) were available. For the period between March and July 2011 they found a correlation of 0.968 with daytime radiosonde measurements. Like the STRAT2D method, the STRAT+ method uses Canny edge detection to detect gradients in the lidar measurements. The difference with the STRAT2D method is that the selection of right gradient as MLH is supported by multiple surface meteorology and turbulence measurements. Also, the variance method is used to get a first (rough) estimate of the MLH. Because the Pathfinder method performed better than the STRAT2D method, we wanted to compare the results of the Pathfinder method to this new STRAT+ method. Although these observations are taken by a lidar similar to the UV-lidar at Cabauw, application of the Pathfinder method was not successful. In many of the cases, attenuation at the ground was stronger than the signal decrease at the MLH. Due to its proximity to Paris, this could be caused by the pollution emitted by the city. An example is given in figure 5.17. Consequently, the Pathfinder algorithm classifies these gradients as MLH and is unable to follow the gradients of the real MLH. This problem might be solved by applying a correction to the measurements for the molecular attenuation.

### 5.5.3. Doppler lidar

A third attempt to test the Pathfinder algorithm was to apply it to a HALO Photonics Doppler lidar located at Chilbolton operated by the University of Reading. This lidar measures elastic backscatter, but also retrieves simultaneous Doppler data by additional measurements at an oblique angle. A method proposed by Harvey et al. (2013) uses the vertical velocities of the Doppler measurements to derive boundary layer types and, as a part of that, also MLH. Because this Doppler method uses a different approach it is ideal for comparison against the Pathfinder method.

The Doppler lidar uses an infrared laser with a wavelength of 1.55 µm. Because of that molecular scattering can be ignored and the measured backscatter is almost completely due to aerosols or cloud particles. There is no molecular attenuation of the lidar signal like in the UV-lidar measurements and low aerosol FA air can be easily distinguished. The data has a temporal resolution of 30s and a vertical resolution of 36m.

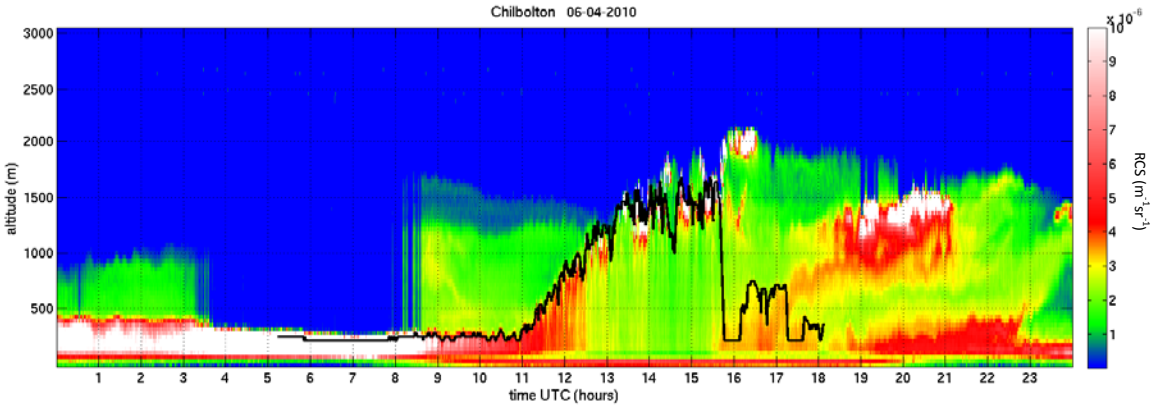


***Figure 5.18. RCS of HALO Doppler lidar together with successful Pathfinder MLH estimate at Chilbolton on 6 April 2010. Due to the relatively long wavelength, molecular backscatter can be ignored.***

As can be seen in figure 5.18, the signal is strong enough to penetrate the complete mixing layer and SNR is sufficient for the Pathfinder method to track MLH for this lidar. Because the lidar signal in the FA is low, gradients on top of the residual layer are relatively large, but with the right set of parameters, the guiding restrictions excluded most of these additional gradients. Although the resolution of this lidar is different from the ALS450, the Pathfinder method can be used to derive MLH from the Doppler lidar observations. Unfortunately, timeseries of MLH derived by the Doppler method were not (yet) available and a comparison could not be made.

## 5.6. Diurnal and annual cycles of the MLH

As mentioned in the introduction of this thesis, lidar observations can be used to improve weather prediction and climate modeling. Because of the high resolution of these measurements, MLH climatologies derived from lidar do not only give information of annual cycles but also diurnal cycles. Here, we will show results based on the data acquired with the Pathfinder method for the full year-comparison described in section 5.2. Although the timeseries are not long enough to produce reliable statistics, they can give an indication of the average state of the MLH in Cabauw.

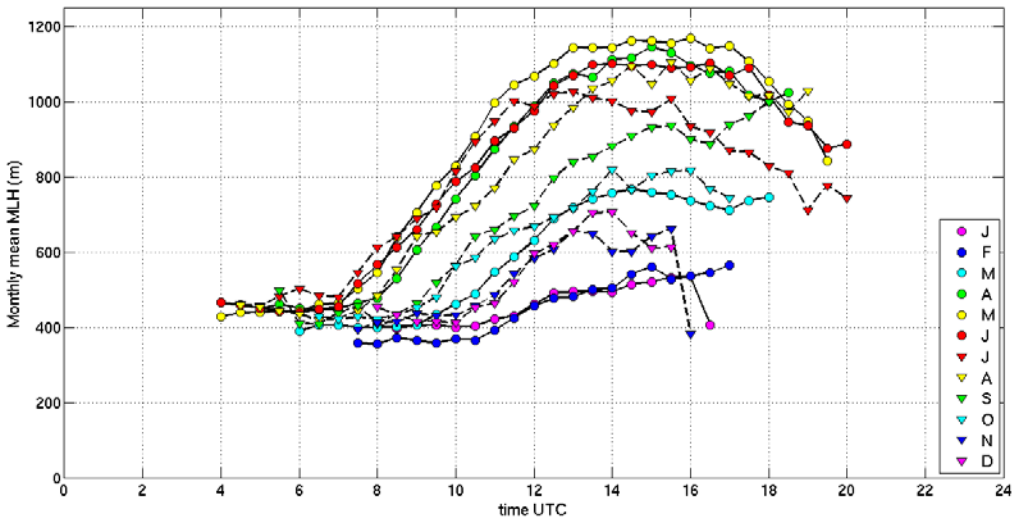


***Figure 5.19. Monthly mean MLH during the daylight period at Cabauw.***

Figure 5.19 shows monthly mean MLH during the daylight period. These averages are based on observations of the ALS450 UV-lidar at Cabauw in 2010, 2011 and 2012. However, in 2011 and 2012 no measurements were taken in July, August and September and the averages in these months are based on 2010 only. Added to of that, 2011 misses observations in December and 2012 misses observations in May and June.

As expected, both a diurnal and an annual cycle are visible in the average MLH. As expected, average MLH is relatively low in autumn and winter with heights between 350 and 700 meters. In summer, MLH is substantially higher and reaches up to average values of 1200 meters. Although there is a link with average daylight periods, highest MLHs are found in spring and the beginning of summer, with May as the month with highest overall MLH. In July and August MLH is considerably lower, despite similar daylight periods as April and May. Also, July and August are the months with the highest average temperatures.

Clearly visible is the diurnal cycle of the MLH. For all months, MLH is between 350 and 500 meters at sunrise. Slightly higher values are found in spring/summer than in autumn/winter. All months display a rapid growth of MLH between 8 and 12 UTC. After that, MLH levels off and remains roughly the same for the remainder of the day. The abrupt breakdown of the MLH in the afternoon is not visible in the monthly means. For some months, e.g. May, June and July, MLH decreases slightly in the afternoon. It might be that the afternoon breakdown is indeed not that abrupt or does not always occur before sunset. Another reason could be the Pathfinder algorithm erroneously keeps tracking the residual layer in the absence of a sufficiently strong gradient on the young NBL.

Due to numerous reasons the maximum height of the ML might not be reached at the same time every day. Therefore, averaging MLH characteristics like in figure 5.19 implies a lower ML than typically observed. For example, on one day MLH reaches its maximum around 12 before a cold front passes so MLH decreases again. On another day, heavy fog could persists and delay ML growth. But despite the delay, MLH keeps increasing in depth until late in the afternoon. Averaging these days might give the indication of a lower maximum extent of MLH during the day because the two maxima are cancelled out.

A better indication of the depth of the ML in Cabauw is given in figure 5.20. Here, the maximum value of MLH is taken for each day regardless of the time of the day it occurred. These values are

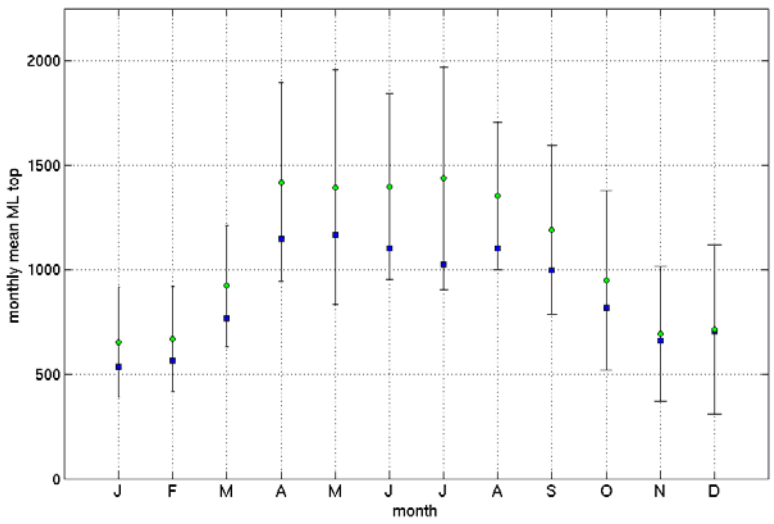


***Figure 5.20. Overview of monthly mean ML top (green). As a comparison, monthly maximum values of the monthly mean diurnal cycle are plotted as well (blue).***

then averaged per month (green). Errorbars of $\pm 1\sigma$ are added to give an indication of the variability in maximum MLH extend in a month. As a comparison, the maximum values of monthly mean values (shown in fig 5.19) are plotted in blue.

Again a clear annual cycle is observed in monthly mean ML top, with highest values of MLH in spring and summer. Values are substantially higher in spring and summer months, with a maximum of 411m in July. During the autumn and winter months, differences are smaller, with a minimum of only 7m for December. This distinction is associated to the absence of a clear diurnal cycle in autumn and winter.

# 6. SUMMARY AND CONCLUSIONS

## 6.1. Summary

Many different instruments are available to derive MLH, like radiosonde, windprofiler and lidars or ceilometers. Here, we focused on lidar observations because of the high resolution measurements and the potential of a large network of instruments for MLH observations. Detection of MLH by lidar is based on the difference in aerosol concentration between the mixing layer and the free atmosphere. However, the vertical gradients on top of the ML have to be separated from interfering features like residual layers and clouds.

Several methods exist to derive MLH from lidar observations. Examples are the gradient, variance, wavelet covariance transform methods. A more advanced method is the STRAT2D method (Morille et al., 2007), which is designed to be applied to different lidars. The code of this method was made available in open source to encourage others to apply the method and share results. Therefore, an analysis of this method was included in this research.

A common feature in the existing methods is that MLH is derived for each timestep individually, which allows for large jumps in the MLH between subsequent timesteps. These jumps are not consistent with the character of the ML which evolves rather gradually. To provide a more physically correct MLH estimate, a new method was proposed called 'Pathfinder'. This method evaluates multiple timesteps simultaneously to prevent these large differences between timesteps. Graph theory is applied together with Dijkstra's (1959) shortest path algorithm to imitate the continuous character of the MLH.

In the Pathfinder method, a full day of lidar measurements is divided into time windows of 15 minute and translated into a graph with vertices representing each individual measurement. To estimate MLH one point is chosen for each timestep. The vertical gradient corresponding to a certain measurement point is used to assign a weight to the vertex inversely proportional to the gradient. This way, the path with the lowest total weight will contain as much strong gradients as possible and will be a good estimate for the MLH. To mimic the gradual evolution of the MLH, the distance between subsequent points is restricted. The threshold used for this is a maximum growth rate of 2,5 $ms^{-1}$. Between the first and last timestep of a time window this threshold is lowered to 1 $ms^{-1}$. To guide the shortest path algorithm, a set of guiding restrictions is used. Features like clouds, strong negative and positive gradients are used to exclude parts of the observations from the searching range for MLH.

The new method is mainly applied to the observations of the LEOSPHERE ALS450 UV-lidar located at Cabauw. Results are shown for different weather conditions: a clear sky-day, a day with clouds and days with precipitation.

As shown with the clear-sky cases, the guiding restrictions make a good pre-selection and exclude large parts of the additional gradients of the residual layer. This allows the shortest path algorithm to track the exact evolution of the MLH in high resolution. In cases the guiding restrictions do not exclude all additional gradients, a jump to another layer of high gradients is (partly) prevented by the shortest path algorithm itself. For such a transition several measurement points with a low gradient have to be included in the path, increasing the total weight of the solution. A jump cannot be prevented completely if the additional gradients are strong enough to compensate for the extra weight for the jump.

Clouds can be a good indicator for MLH height, but the high backscatter on the cloud droplets cause a negative gradient typically an order of magnitude larger than gradients associated with differences in aerosol concentration. Because of these strong gradients, the solution found by the algorithm is

drawn to cloud tops. In case of a cloud layer above the ML, guidance by the restrictions is necessary to divert the algorithm to the MLH. However, these restrictions are not needed for every time step. Because the algorithm looks for series of connected timesteps, a restriction on one timestep keeps the algorithm on the right solution for several timesteps before and after that timestep.

During rain it is difficult to derive a MLH, because of the attenuation of the lidar signal by water on the instrument. During precipitation events not reaching the surface, it was visible that the downdraft of a rainshower lowered the MLH. The algorithm is able to correctly follow this decrease in MLH as long as the precipitation evaporates before reaching the overlap region. Otherwise, there is no negative gradient to assign MLH to. The top of the precipitating cloud will be calculated as MLH instead, although it is not the actual MLH.

Because of the high temporal resolution of the lidar observations, changes in MLH by individual thermals are dominant in our results. The typical spatial scale of the thermals is in the order of several hundreds of meters up to a kilometer. To compare results to other instruments with a similar resolution, the distance between them should not be greater than this typical timescale. Otherwise, the instruments would observe different thermals and different MLH. This severely limited the options to test the results of the Pathfinder algorithm. However, the 2008 EUCAARI-IMPACT campaign held at Cabauw provided collocated datasets of lidar, windprofiler and radiosonde observations. Unfortunately, the overlapping period was only 12 days. The agreement between the Pathfinder and the windprofiler was excellent ($R^2 = 0.96$), but substantial differences were found between Pathfinder and radiosonde. In the early morning MLH usually was too low to be well detected by lidar. But during the morning transition (radiosondes at 10 UTC), the radiosonde method yielded incorrect results. An explanation could be that this method ignores the effects of entrainment of ML air into the rising thermals.

The lack of longer MLH time series and the limitations of the radiosonde method forced us to create a manual dataset for MLH to compare the results of applying the Pathfinder method to a full year of lidar measurements. Although these two methods are not completely independent, it provided a quantitative measure of the performance in different weather conditions. Again, the Pathfinder method agreed well to the manual estimates ($R^2 = 0.90$, increasing to $R^2 = 0.95$ when only selecting the results with a good backscatter ratio).

Our new method outperformed the STRAT2D method for both the IMPACT period as well as the full-year comparison ($R^2$= 0.74). The first difficulty of the STRAT2D method are the large jumps in MLH. These are caused by gradients in the residual layer or inhomogeneities within the ML. In addition, the STRAT2D method was not able to pinpoint an estimate for MLH on days with low aerosol concentrations in the ML. Without a sufficient difference between FA and ML, the criterion based on the backscatter ratio rejected these estimates.

By limiting the vertical range between subsequent timesteps, the searching range is determined by the solution itself. However, the starting point and the size of the time windows also affect the searching range. A sensitivity study was performed to check the stability of the solution for these parameters. Shifting the starting point or size had only a limited effect on the derived MLH, with average correlations above $R^2 = 0.96$ (the lowest overall correlation was $R^2 = 0.82$). Deviations did occur, but all additional calculations gave the exact same MLH for at least 75% of the timesteps within a day. The average correlation was lowest for shifts of half the window size, because these have the lowest overlap in searching range with the default calculation. Changes in window size have a larger effect on the searching range and correlations were slightly lower. Minimum correlations were about $R^2 =$ 0.85 except for the time window of 10 timesteps (5 minutes) which was too small to be able to track individual thermals correctly.

## 6.2. Conclusions

In all, the following conclusions can be drawn from this research:

- Simultaneous evaluation of multiple timesteps in the Pathfinder method prevents jumps between different layers and produces a coherent estimate of MLH evolution during the day. Although the vertical range between timesteps is restricted, the method is capable of tracking rapid variations associated with individual thermals.

- Excellent agreement was found between MLH estimates of the Pathfinder method and windprofiler or manual MLH estimates.

- In all comparisons carried out in this research, the Pathfinder method outperforms the STRAT2D method. This is due to the jumps between layers present in the STRAT2D estimates and the criterion of backscatter ratio used in this method.

- The Pathfinder method can be used for operational use. Typical computation times (1,5 minute for an observations of a full day) are short enough and although multiple timesteps are used simultaneously, time windows can be as short as 15 minutes.

- MLH estimates by radiosonde methods appeared to be of poor quality. This is a point of concern because these methods, mainly the Richardson bulk method, are frequently used to test the performance of lidar methods. Especially during the early morning transition, radiosonde methods overestimate MLH. A possible explanation could be neglecting entrainment of ML air into rising thermals by these methods.

## 6.3. Recommendations

Based on the findings of this research, the following recommendations for future research are proposed:

- Although excellent correlations between the Pathfinder method and other MLH estimates are found in this research, comparisons of longer periods with wind profiler or Doppler lidar are desirable. Comparison of time series at a high temporal resolution provides a more complete overview of the performance of the Pathfinder method at different times of the day.

- Because the MLH estimates of the Pathfinder method are not uniform for different sets of algorithm parameters, additional research can be done to find optimal values of e.g. window size or translation from gradients to graph weights values.

- In theory, the Pathfinder should be applicable to any instrument producing measurements on a resolution similar to lidar. As long as measurement values in the ML are sufficiently different from the FA, the Pathfinder method should be able to track MLH. Further investigation of the performance of the Pathfinder on different instruments is needed to find out whether production of harmonized datasets is possible with the Pathfinder method.

- To further improve the quality of the Pathfinder method, possibilities to integrate other methods into the Pathfinder method should be explored. Currently, the Pathfinder method selects MLH using the vertical gradients in the lidar backscatter signal. Instead, other lidar methods could be used to make a pre-selection of several altitudes in each timestep. This pre-selection could then be combined into a possible evolution of MLH by the Pathfinder algorithm.

# 7. REFERENCES


Angevine, W.M., A.B. White and S.K. Avery (1994), Boundary layer depth and entrainment zone characterization with a boundary-layer profiler, *Boundary-Layer Meteorology,* **68**, 375-385, doi: 10.1007/BF00706797

Angevine, W.M., H. Klein Baltink, F.C. Bosveld (2001), Observations of the morning transition of the convective boundary layer, *Boundary-Layer Meteorology*, **101**, 209-227, doi: 10.1023/A:1019264716195

Baars, H., A. Ansmann, R. Engelmann and D. Althausen (2008) Continuous monitoring of the boundary-layer top with lidar. *Atmospheric Chemistry and Physics*, **8(23)**, 7281–7296. doi:10.5194/acp-8-7281-2008.

Boers, R. E.W. Eloranta and R.L. Coulter (1984), Lidar observations of mixed layer dynamics: Tests of parameterized entrainment models of mixed layer growth rate. *Journal of Applied Meteorology and Climatology*, **34**, 357-375

Dijkstra, E.W., 1959. A note on two problems in connexion with graphs. *Numerische Mathematik*, **1(1)**, 269–271. doi:10.1007/bf01386390.

Eresmaa, N., A. Karppinen, S.M Joffre, J. Räsänen and H. Talvitie, (2006), Mixing height determination by ceilometer. *Atmospheric Chemistry and Physics,* **6**, 1485-1493.

Flamant, C., J. Pelon, P.H. Flamant, P. Durrand (1997), Lidar determination of the entrainment zone thickness at the top of the unstable marine atmospheric boundary layer, *Boundary-Layer Meteorology*, **83**, 247–284

Garratt, J.R. (1992), The atmospheric boundary layer, *Cambridge University Press*, 316pp.

Haeffelin, M., F. Angelini, Y. Morille, G. Martucci, S. Frey, G. P. Gobbi, S. Lolli, C. D. O'Dowd, L. Sauvage, I. Xueref-Rémy, B. Wastine, and D. G. Feist (2010), Evaluation of Mixing-Height Retrievals from Automatic Profiling Lidars and Ceilometers in View of Future Integrated Networks in Europe. *Boundary-Layer Meteorology*, **143(1)**, 49–75. doi:10.1007/s10546-011-9643-z.

Haij, M., W. Wauben and H. Klein Baltink (2007), Continuous mixing layer height determination using the LD-40 ceilometer: a feasibility study, Scientific Report WR 2007-01, KNMI, De Bilt, 102 pp.

Harvey, N.J., R.J. Hogan and H. F. Dacre (2013), A method to diagnose boundary-layer type using Doppler lidar, *Quarterly Journal of the Royal Meteorological Society*, **129**, 1681-1693. doi: 10.1002/qj.2068

Hayden, K.L., K.G. Anlauf, R.M. Hoff, J.W. Strapp, J.W. Bottenheim, H.A. Wiebe, F.A. Froude, J.B. Martin, D.G. Steyn and I.G. McKendry (1997), The vertical chemical and meteorological structure of the boundary layer in the Lower Fraser Valley during Pacific '93, *Atmospheric Environment*, **31**, 2089-2105. doi:10.1016/s1352-2310(96)00300-7

Holzworth, C. G., (1964) Estimates of mean maximum wind depths in the contiguous United States, *Monthly Weather Review,* **92**, 235-242

Hooper, W. P., E.W. Eloranta (1986), Lidar measurements of wind in the planetary boundary layer: the method, accuracy and results from joint measurements with radiosonde and kytoon. *Journal of Applied Meteorology and Climatology*, **25**, 990–1001.

Menut, L., C. Flamant, J. Pelon and P.H. Flamant (1999), Urban boundary layer height determination from lidar measurements over the Paris area, *Applied Optics*, **38**, 945-954. doi: 10.1175/1520-0450(1986)025<0990:LMOWIT>2.0.CO;2

Morille, Y., M. Haeffelin, P. Drobinski, and J. Pelon (2007) STRAT: An automated algorithm to retrieve the vertical structure of the atmosphere from single-channel lidar data. *Journal of Atmospheric and Oceanic Technology*, **24**, 761-775.

Nicolae, D. and C. Talianu (2010), Atmospheric lidar and retrieval of aerosol optical characteristics, Series: Optoelectronic Materials and Devices, Volume 7: Recent advances in Atmospheric lidars, *INOE*, Bucharest, 1-86

Ottersten, H. (1969), Atmospheric Structure and Radar Backscattering in Clear Air, *Radio Science*, **4(12)**, 1179–1193, doi:10.1029/RS004i012p01179.

Pal, S., Haeffelin, M. and Batchvarova, E., 2013. Exploring a geophysical process-based attribution technique for the determination of the atmospheric boundary layer depth using aerosol lidar and near-surface meteorological measurements. *Journal of Geophysical Research: Atmospheres*, **118(16)**, 9277–9295. doi:10.1002/jgrd.50710.

E. Palmen and C. W. Newton (1969), Atmospheric Circulation Systems. Their Structural and Physical Interpretation, *Academic Press*, New York, 606 pp.

Piironen, A. K., and E. W. Eloranta (1995), Convective boundary layer mean depths and cloud geometrical properties obtained from volume imaging lidar data, *Journal of Geophysical Research*, **100(D12)**, 25569–25576, doi:10.1029/94JD02604.

Pul, van, W.A.J., A.A.M. Holtslag and D.P.J. Swart, (1994) A comparison of ABL heights inferred routinely from lidar and radiosondes at noontime. *Boundary-Layer Meteorology*, **68**, 173-191.

Seibert, P., F. Beyrich, S.-E. Gryning, S. Joffre, A. Rasmussen and P. Tercier (2000) Review and intercomparison of operational methods for the determination of the mixing height. *Atmospheric Environment*, **34**, 1001-1027.

Steeneveld, G. J., B. J. H. van de Wiel, A. A. M. Holtslag (2007), Diagnostic Equations for the Stable Boundary Layer Height: Evaluation and Dimensional Analysis. *Journal of Applied Meteorology and Climatology,* **46**, 212–225. doi: 10.1175/JAM2454.1

Steyn, D.G., M. Baldi and R.M. Hoff (1999) The detection of mixed layer depth from lidar backscatter profiles. *Journal of Atmospheric and Oceanic Technology,* **16**, 953-959.

Stull, R.B., (1988) An Introduction to Boundary Layer Meteorology. *Kluwer Academic Publishers*, Dordrecht, 665 pp.

Stull, R.B., (1976b) Mixed layer depth model based on turbulent energetics, *Journal of the Atmospheric Sciences*, **33**, 1268-1278

Vogelezang, D.H.P. and A.A.M. Holtslag (1996), Evaluation and model impacts of alternative boundary-layer height formulations, *Boundary-Layer Meteorology*, **81**, 245-269.

Wiegner, M., S. Emeis, V. Freudenthaler, B. Heese, W. Junkermann, C. Münkel, K. Schäfer, M. Seefeldner, and S. Vogt (2006), Mixing layer height over Munich, Germany: Variability and comparisons of different methodologies, *Journal of Geophysical Research*, **111**, D13201, doi:10.1029/2005JD006593.

Zilitinkevich, S., and A. Baklanov (2002), Calculation of the height of the stable boundary layer in practical applications, *Boundary-Layer Meteorology*, **105**, 389-409